MASTER

Detection and classification of cerebral emboli using radio frequency-based transcranial Doppler echography

Lipperts, M.G.A.

Award date:
2010

Detection and Classification of Cerebral Emboli using Radio Frequency-based Transcranial Doppler Echography

Master's Thesis
M.G.A. Lipperts
September 2006–September 2007
MRL/TPM 2007-10

Eindhoven University of Technology
Department of Applied Physics

University hospital Maastricht
Department of Cardiothoracal Surgery

Supervisors:
Prof. dr. ir. K. Kopinga
Prof. dr. ir. A.P.G. Hoeks
Prof. dr. W.H. Mess
Ir. L. Sauren

Abstract

The possibilities of radio frequency based transcranial Doppler (TCD) methods for emboli detection are explored, and compared to traditional Doppler audio methods. The focus was on the discrimination between solid and gaseous emboli, quantifying air-showers and detecting low-intensity micro-embolic signals (MES). A numerical model has been developed based on the Rayleigh-Plesset equation, to investigate the behaviour of small air bubbles when insonified with ultrasound. It was found that a certain diameter range of gas bubbles continue to oscillate at their resonance frequency after the driving ultrasound pulse ended. This effect can possibly be used to distinguish air bubbles from solid scatterers.

To quantify air-showers a counting algorithm has been developed, and tested using 20 three second recordings. 277 Of the 388 MES were detected by the algorithm, while only 6 events were falsely classified as MES, yielding a sensitivity of 0.7 and a positive predictive value of 0.96. These values can be improved by developing a more sophisticated shape recognition algorithm.

To detect low-intensity MES a flow phantom set-up has been built, in which small solid particles were introduced. The smallest ($\sim 50\,\mu m$) particles were visible in the RF amplitude plots, and their amplitude approaches the amplitude of blood speckle, which is believed to be the detection limit. It was concluded that in all areas, RF based TCD methods can be used as a substitute or even improvement of traditional Doppler audio methods.

Contents

Chapter 1

Introduction

1.1 Cerebrovascular Anatomy

Transcranial Doppler echography (TCD) uses ultrasound to monitor cerebral blood flow and can be used to detect cerebral emboli. The motion of blood is the base of this technique. It will be explained in more detail in the next chapter(s). The thin temporal window above the cheekbone in front of the ears is used as a transmission window, since a thicker human skull blocks the transmission of ultrasound. In almost all people the window is so thin that the transmission is high enough to allow the use of TCD. Through this window the Middle Cerebral Artery (MCA) is most commonly insonified. However, also the Posterior and Anterior Cerebral Artery (PCA and ACA) can be measured, see figure 1.1. The Internal Carotid Artery (ICA) branches off in the large MCA and the smaller ACA. The right and left ACA are connected through the Anterior communicating Artery (AcomA), and they are connected to the PCA through the Posterior communicating Arteries (PcomA). The PCA originates from the vertebral artery. The circle formed by both ACAs, PCA and the communicating arteries is called the Circle of Willis, and plays an important role in the blood supply of the brain, especially when one of the carotid arteries is occluded partially or completely.

1.2 Clinical Relevance

The highest percentage of all surgeries is cardiothoracic. During those procedures (mostly coronary artery bypass grafts (CABGs), and cardiac valve operations (CVOs)) the occurrence of microemboli is inevitable. The relation between the number of emboli and postoperative neurovascular damage has been studied extensively in several clinical studies [11, 14, 12]. The consensus is that larger embolic loads cause greater neurological damage. However, it is also shown [12] that the number of emboli is not the most important factor influencing the neurological outcome. Among the risk factors are age, heart disease and previous cardiac operations. Also the effect of the duration of cardiac bypass cannot be excluded. Several reports have shown a correlation between emboli and neurological deficits, but the nature of the emboli can prove to play a crucial role. Neville et al. [12] state that, although in CVOs emboli are much more numerous than in CABGs, the neurological outcome from patients undergoing either of the two procedures does not differ significantly. It is assumed that the majority of emboli during CVOs is gaseous, as a consequence of the fact that the heart is

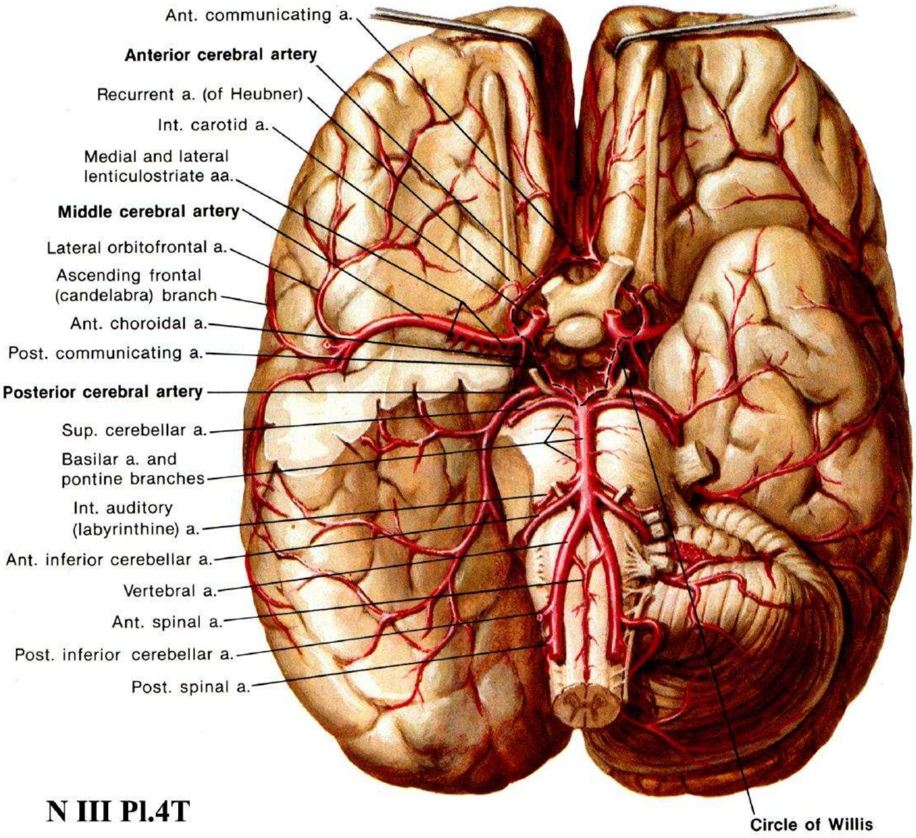

Figure 1.1: Cerebral Anatomy, showing MCA, ACA, PCA and other cerebral arteries [1].

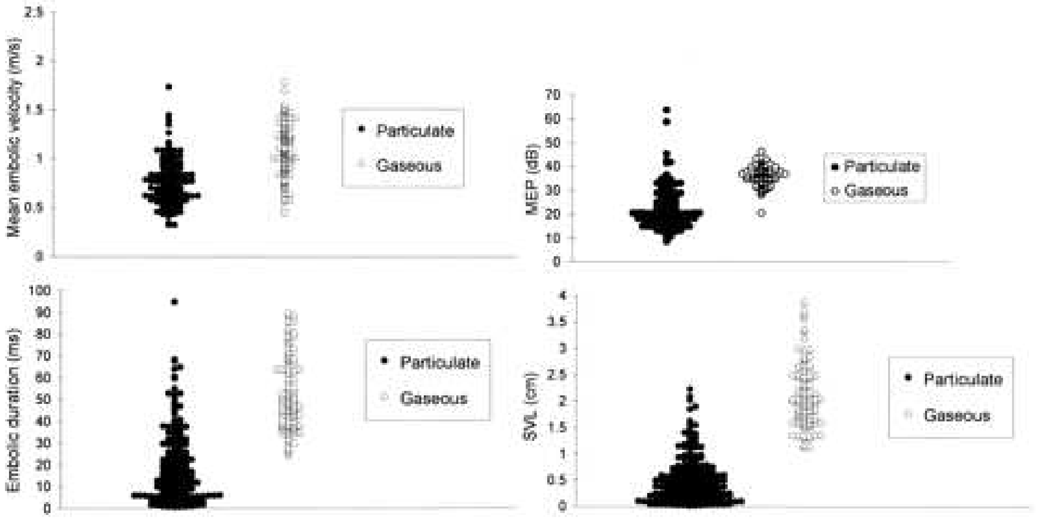

Figure 1.2: Distribution of 4 parameters for gaseous and solid emboli found by [16].

opened during these procedures. In CABGs the percentage of solid emboli is higher, which leads to the hypothesis that solid emboli are the main cause of neurovascular damage. The effect of gaseous emboli, however, remains unclear to this point. Muth et al. [11] investigated the influence of gaseous emboli on brain physiology and they state that also air can cause some damage by oedema formation, which could lead to cognitive disorders. Clinically, however, no data exists of the relation between the amount of gaseous emboli and the severity of cognitive decline, which could be due to the fact that no accurate methods exist yet to count large emboli-densities.

The difference between gaseous and solid emboli is also of interest for research purposes, for instance whether or not administering oxygen will reduce the amount of gaseous emboli in patients with mechanical heart valves. These observations make it worthwhile to develop a method to reliably distinguish between solid and gaseous emboli. The development of such a method is one of the main goals of this project, together with the development of a method to count large amounts of emboli.

1.3 Previous Work

The last 15 years many attempts have been made to systematically distinguish between gaseous and solid emboli and to automatically detect them. So far, however, the results have not been very promising, especially in the former field.

Various principles were used to distinguish between the two types of emboli. Smith et al. [16] compared 4 different methods in their paper. They tried to observe differences in embolic duration, embolic velocity, relative signal intensity increase, and sample volume length. The results are shown in figure 1.2, and it can be seen that using these four parameters a complete distinction can never be made. Based on signal volume length (which is equal to velocity

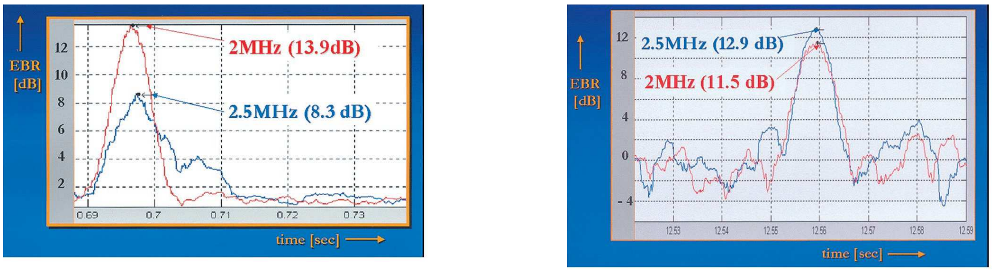

(a) a gaseous embolus

(b) a solid embolus

Figure 1.3: Results of using a multifrequency TCD system. The amplitude of a gaseous embolus will decrease with increasing frequency, whereas the amplitude of a solid embolus will increase with increasing frequency. [15]

times duration) the best approximate distinction can be made, but also in this case there is some overlap between signals from gaseous and particulate emboli.

It appears that a somewhat more complicated approach is required to reach a higher level of specificity. Russell and Brucher [15] use a different approach. They use a multifrequency TCD system, in which simultaneously a 2 MHz and a 2.5 MHz pulse are emitted. Two of their results are shown in figure 1.3. Their hypothesis is that the scattering cross section of gaseous emboli decreases with increasing frequency while for solid emboli the cross section increases. This holds for solid particles (it will be shown in the next chapter that the cross section is proportional to the fourth power of frequency), whereas for gaseous emboli the behaviour will be more complicated. Furthermore Evans et al. showed that beam distortion due to the skull can influence the intensity of embolic signals [3]. The suggestion of frequency dependence of the embolic signals was also made by Moehring and Klepper [18].

In a different paper [10] Moehring proposes his Embolus to Blood Ratio (EBR) model to size emboli in blood. However, this is done only for solid particles based on calculations of the backscatter cross section for solid microspheres. He uses two different insonation frequencies, and the values of the EBR at both frequencies would be an unambiguous representation of the diameter of the embolus. Their results are given in figure 1.4. The solid curve represents the theoretical model. The scattered points indicate the experimental values. It can be seen that although the spread of the results is not too large, it is hard to predict the size of the embolus, because the curve is not monotonous where the majority of the experimental points is found. Although this method could possibly prove to be useful in sizing solid emboli, it cannot discriminate between solid and gaseous emboli.

The first to use a different approach was Palanchon in 2002 [13], who used the non-linear properties of gas bubble scattering to make a distinction between gas and solids. She detects sub- and ultraharmonic components of the signal scattered by different air bubbles, see figure 1.5. The advantage of this method is that, when these components are observed, it is certain that the embolus is gaseous. The disadvantage is also obvious, and arises from the fact that, to see these components of the signal, the bubble has to be insonated close to its resonance frequency. For typical bubbles this resonance frequency is below 1 MHz, whereas

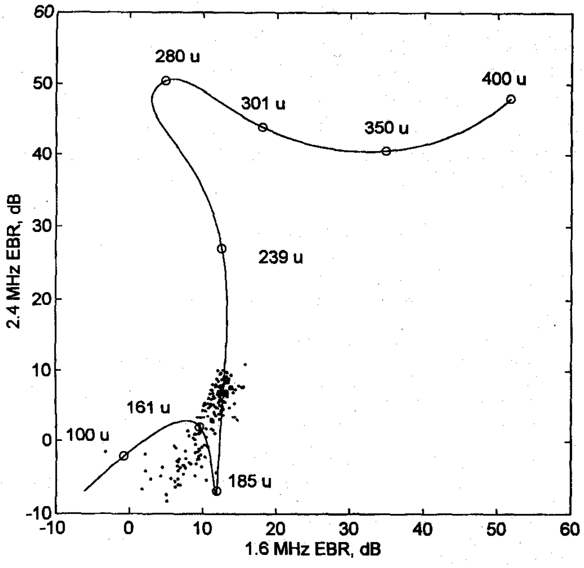

Figure 1.4: Results of EBR model. The line indicates the EBR values found using the theoretical model, the somewhat scattered points indicate the values found in an in vitro experiment [10].

Doppler frequencies accepted by the Food and Drug Authority (FDA) are around 2 MHz. Furthermore, a priori the bubble size and thus its resonance frequency is unknown, which makes it in principle impossible to insonate an unknown bubble at its resonance frequency. However, when lower insonation frequencies are used, Palanchon showed that it is possible to detect sub- and ultraharmonics in the signal of bubbles within a certain range. The maximum intensity is reached when a frequency twice the resonance frequency is used. Although this method seems promising, practical problems prevent it to be used clinically.

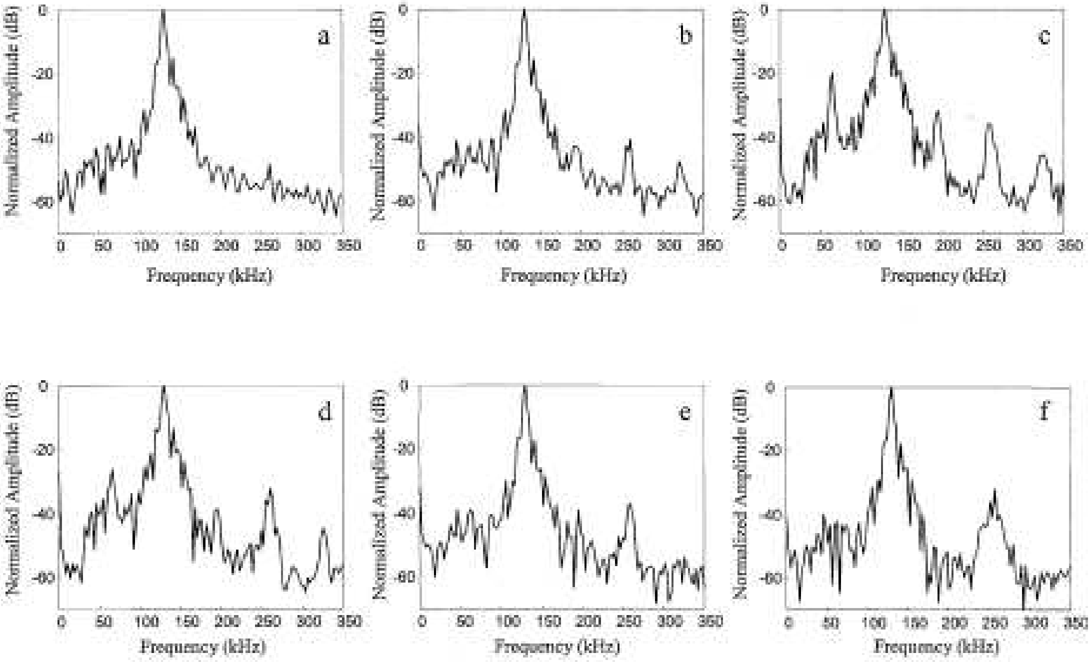

Figure 1.5: Sub- and ultraharmonic components in the scattered echo for different bubbles [13].

Chapter 2

Theory

2.1 General Acoustics

Ultrasound propagation is, like any other acoustic wave, governed by the acoustic wave equation:

$$\frac{\partial^2 p}{\partial^2 x} - \frac{1}{c^2}\frac{\partial^2 p}{\partial^2 t} = 0. \tag{2.1}$$

Here p is the acoustic pressure, x is the longitudinal place coordinate, t is time, and c is the (phase)velocity of the sound in the medium of consideration. The solution of the wave equation is of the form:

$$p = p_A \exp[i(\omega t \pm kx)], \tag{2.2}$$

where p_A is the pressure amplitude, ω is the angular frequency, and k is the wave number ($= 2\pi/\lambda$). Ultrasound is characterized by a frequency ($f = \omega/2\pi$) above the human audible range ($>$ 20 kHz). In "simple" waves there is a linear relation between ω and k: $c = \omega/k$. In some cases (high frequencies, high pressure amplitudes), c can be a function of frequency and also of the phase of the pressure wave. This will be considered in a later section.

2.1.1 Acoustic impedance

An important parameter in acoustics is the acoustic impedance, Z. Impedance is defined as the ratio of a driving force to the velocity response on this force. In acoustics the driving force is the acoustic pressure, and the particle velocity is the response hereto. Hence:

$$Z = \frac{p}{\dot{\epsilon}}, \tag{2.3}$$

where p is the acoustic pressure, and $\dot{\epsilon}$ is the first time derivative of the particle displacement. For simple waves the acoustic impedance is given by

$$Z = \rho c, \tag{2.4}$$

where ρ is the material density, and c is the speed of sound again in this medium. The derivation of this equation is given in [17].

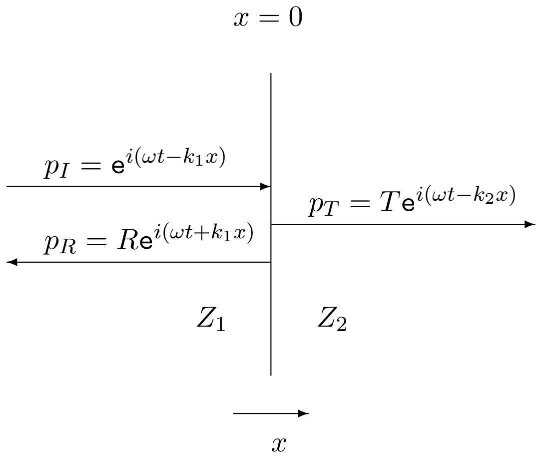

Figure 2.1: Pressure waves at an interface between 2 media.

2.1.2 Intensity

The energy density of a sound wave is just as in a spring-bob system a combination of potential and kinetic energy. Again without proof the total energy density per unit volume is given by:

$$\phi = \frac{1}{2}\rho|\dot{\epsilon}|^2_{\max}. \tag{2.5}$$

The amount of energy flowing through an area A in a time Δt is the total energy density multiplied by $Ac\Delta t$, and therefore the intensity of the plane wave will be:

$$I = \phi c = \frac{1}{2}\rho c|\dot{\epsilon}|^2_{\max} = \frac{1}{2}Z(\frac{p_A}{Z})^2. \tag{2.6}$$

2.1.3 Reflection

At an interface of two media with different acoustic impedances, ultrasound waves will be partially reflected. The situation is shown as in figure 2.1. The normalized incident pressure wave is denoted:

$$p_I = \mathrm{e}^{i(\omega t - k_1 x)}. \tag{2.7}$$

The reflected and transmitted pressure wave are respectively

$$p_R = R\mathrm{e}^{i(\omega t + k_1 x)}, \tag{2.8}$$

$$p_T = T\mathrm{e}^{i(\omega t - k_2 x)}. \tag{2.9}$$

Here R and T are the ratio of the reflected and transmitted pressure amplitude to the incident pressure amplitude. At the interface $x = 0$ the pressure has to be continuous:

$$P_I + P_R = P_T \rightarrow 1 + R = T. \tag{2.10}$$

Also the particle velocities must be continuous at the interface, since the media are and stay in contact:

$$\frac{1}{Z_1}(1 - R) = \frac{1}{Z_2}T, \tag{2.11}$$

Table 2.1: Reflection coefficients for some useful interfaces.

Reflecting interface	Ratio of reflected to incident wave amplitude	Percentage energy reflected
Bone/fat	0.70	48.9
Bone/muscle	0.64	41.2
Soft tissue/water	0.05	0.23
Soft tissue/air	0.9995	99.9
Soft tissue/PZT crystal	0.89	80.0
Muscle/blood	0.03	0.07

using equation 2.3. Solving the two equations for R gives the relative amplitude of the reflected pressure wave:

$$R = \frac{Z_2 - Z_1}{Z_2 + Z_1}. \tag{2.12}$$

In table 2.1 some relevant reflection coefficients are given.

2.1.4 Attenuation

Due to different sources of relaxation (thermal, structural), a traveling ultrasound wave will be attenuated by tissue. These relaxation processes will cause a phase difference between pressure and velocity response. From equation 2.3 it can be seen that this will give a complex acoustic impedance. In [17] it is shown that a complex acoustic impedance also implies a complex wave number, $k = q + ib$. Substituting this in equation 2.2 gives the harmonic solution with a damping term: $p = p_0 \exp[i(\omega t \pm qx) - b(\omega)x]$. Now the frequency dependent amplitude attenuation coefficient (C_{AA}) can be defined as:

$$C_{AA} = \frac{20}{x} \log_{10}\left(\frac{p_0}{p}\right) = 20b \log \mathsf{e}. \tag{2.13}$$

C_{AA} is usually given in dB/(cm·MHz). Some useful values are given in table 2.2.

2.1.5 Non-linear Propagation

As stated before in this section, in some cases the sound velocity is not a constant. In general the sound velocity is proportional to the stiffness of the corresponding medium. This stiffness changes with pressure, so that higher pressure means larger stiffness. This means that the compression portions in an ultrasound wave travel faster than the rarefaction parts, which is shown in figure 2.2(a). This distortion increases until the positive half cycle catches up with the negative and a shock wave is formed. Further from the source, high frequency components are attenuated more and the wave returns to its original shape, but strongly attenuated. The wave form from a TCD unit is shown in figure 2.2(b), where also non-linear behavior can be observed. Although the pressures used in TCD are high enough to lead to non-linear propagation, research done by [8] shows that the error in velocity estimations resulting from the distortion is relatively small.

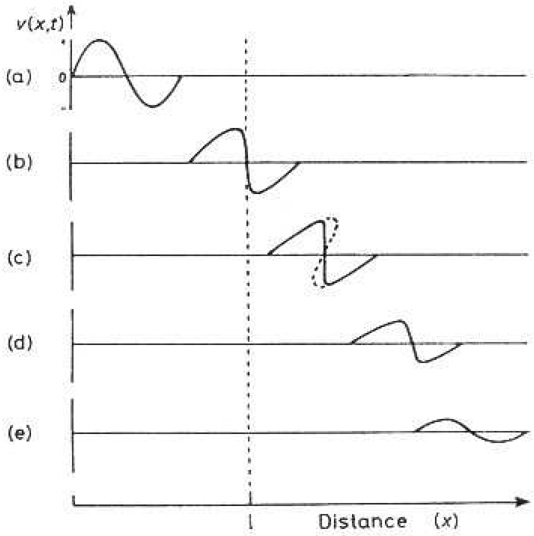

(a) Evolution of a sinusoidal wave launched at distance $x = 0$ and time $t = 0$ in a non-linear, weakly attenuating medium. In (b) a shock front forms, which increases in strength (c). High frequency components are attenuated (d) and the wave returns to an attenuated sine wave (e)[4].

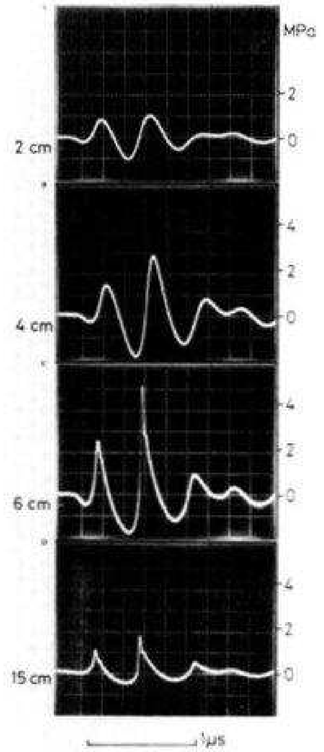

(b) Distortion of a 2 MHz ultrasound pulse in water. The shapes are recorded 2,4,6 and 15 cm from the source [4].

Figure 2.2: Forming of a distorted wave (a) and a distorted 2 MHz ultrasound pulse (b).

Table 2.2: Attenuation coefficients for some common tissues in dB/cm, at 2 MHz.

Tissue	Attenuation coefficient (dB/cm)
Blood	0.4
Muscle	3.0
Brain(adult)	1.6
Brain(infant)	0.6
Bone	20
Fat	1.2
Water	0.004
Soft tissue	1.4

2.1.6 Scattering

When an ultrasonic wave propagates through an inhomogeneous medium, (i.e.: a medium with particles with sharp boundaries and/or different physical properties (acoustic impedance) than the surrounding medium), the wave will be scattered by those particles. The scattered wave can in turn be scattered again by another particle, but in cases where the number of particles is not too large these repeatedly scattered waves can be neglected. The total scattered field can now be regarded as the superposition of the scattered waves from single scatterers.

Here the scattering of particles smaller than the wavelength of the ultrasonic wave in the surrounding medium is considered, which is known as "Rayleigh scattering". In this case the scattering parameter, defined as kR, is much smaller than 1. Here k is again the wave number, and R is the particle radius. Now the particles can be regarded as small spheres, so the logical choice is to do any further calculation in spherical coordinates. As depicted in figure 2.3 the potential of the incident wave (in negative x-direction) as seen from the point of observation, A, will be of the form:

$$\phi(r,\theta,t) = \phi_{\mathtt{max}} \exp(i\omega t)\exp(ikr\cos\theta), \tag{2.14}$$

since $x = r\cos\theta$. Then the factor $\exp(ikr\cos\theta)$ can be expanded in a series of spherical functions, yielding for the potential:

$$\phi = \phi_{\mathtt{max}} \exp(i\omega t)\sum_{m=0}^{\infty}(-1)^m(2m+1)P_m(\cos\theta)J_m(kr), \tag{2.15}$$

where $P_m(\cos\theta)$ are Legendre polynomials, and $J_m(kr)$ is a Bessel function of order m.

Similarly the scattered wave can be written as a superposition of spherical waves emanating from the origin:

$$\psi = \exp(i\omega t)\sum_{m=0}^{\infty} a_m P_m(\cos\theta) f_m(ikr)\frac{\exp(ikr)}{r}, \tag{2.16}$$

where far from the scatterer ($kr \gg 1$) the function f_m will be equal to 1, and the coefficients a_m are found from boundary conditions. In the case of solid particles in a liquid, which is the case for solid emboli, the particle velocities in radial direction at the boundary of the particle

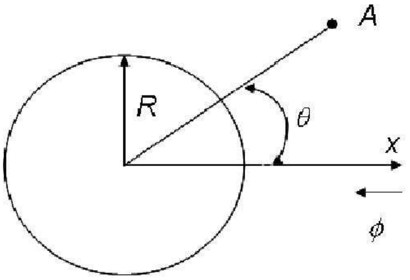

Figure 2.3: Spherical coordinate system with particle of radius R and point of observation A.

are 0, since the solid scatterer is assumed to be incompressible. This leads to the following boundary condition:

$$\left.\frac{\partial\phi}{\partial r}+\frac{\partial\psi}{\partial r}\right|_{r=R}=0. \tag{2.17}$$

Now for every m an expression is found for a_m, which can be substituted back into 2.16. The potential of the scattered wave now becomes (taking the sum of the first 2 spherical harmonics):

$$\psi(\theta,r,t)\simeq-\frac{k^2R^3}{3r}\left(1+3/2\cos\theta\right)\cos(\omega t-kr). \tag{2.18}$$

The derivation of this equation is found in [19].
For the intensity, which is proportional to the square of the amplitude, the following expression is found:

$$I=I_0\frac{\omega^4R^6}{9c^4r^2}\left(1+\frac{3}{2}\cos\theta\right)^2. \tag{2.19}$$

This equation shows that the scattered intensity is the highest for $\theta=0$, which corresponds to backscattering.
The method described here can also be applied for gaseous emboli, just by changing the boundary conditions. However, it is more instructive to use another approach, which is shown in section 2.2.

2.2 Gas Bubble Acoustics

2.2.1 Determination of the Bubble Resonance Frequency

The wall motion of gas bubbles can be regarded as the motion of a harmonic oscillator. Considering a mass-spring system, the two elements comprising the harmonic motion are a restoring force (spring) and the inertia of the mass. In a gas bubble, the restoring force is the

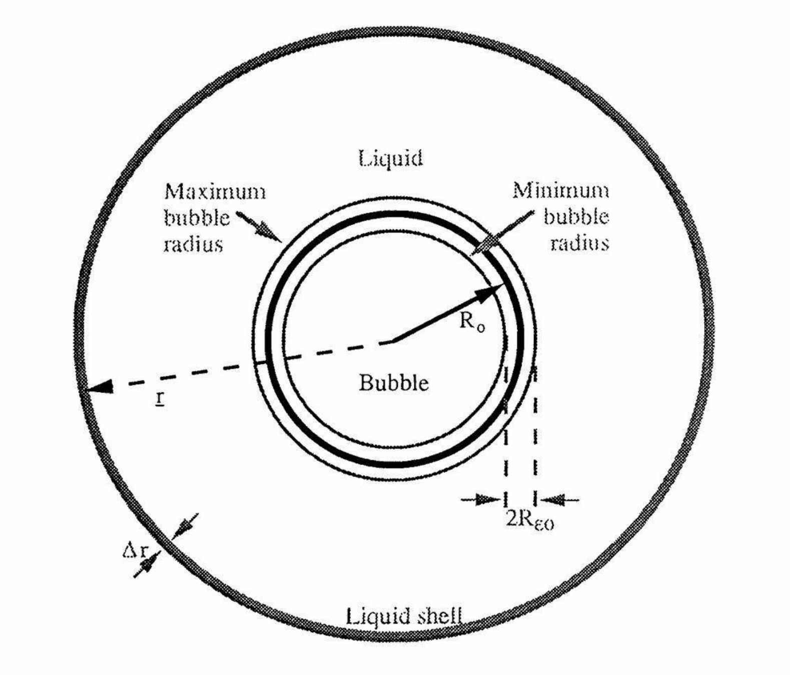

Figure 2.4: Bubble of radius R_0, undergoing small linear oscillations of amplitude $R_{\epsilon 0}$, surrounded by spherical shells of liquid [17].

pressure of the gas inside the bubble and the inertia is provided by the surrounding fluid. The resonance frequency of air bubbles can be found by equating the maximum potential energy $\phi_{\mathtt{p,max}}$ to the maximum kinetic energy of the surrounding fluid $\phi_{\mathtt{k,max}}$. The kinetic energy of the fluid can be found from (see also figure 2.4):

$$\int_R^\infty (4\pi r^2 \rho \, dr) v_r^2, \tag{2.20}$$

where v_r^2 is the radial component of the liquid flow velocity. The velocity profile can be found, assuming the liquid is incompressible, from the continuity equation in spherical coordinates, assuming spherical symmetry:

$$\nabla \cdot \vec{v} = \frac{1}{r^2}\frac{\partial}{\partial r} r^2 v_r = 0, \tag{2.21}$$

which with boundary conditions $v(R) = \dot{R}$ and $v(\infty) = 0$ has solution:

$$v_r(t) = \frac{\dot{R}R^2}{r^2}. \tag{2.22}$$

Substituting this expression in equation 2.20 and assuming harmonic motion, which means that the maximum value of the kinetic energy is found at the equilibrium position $R = R_0$ and $\dot{R} = i\omega_0 R_{\epsilon 0} \mathrm{e}^{i\omega t}$, gives a maximum value of the kinetic energy:

$$\phi_{\mathtt{k,max}} = 2\pi R_0^3 \rho (R_{\epsilon 0}\omega_0)^2. \tag{2.23}$$

The maximum potential energy is equal to the work done by the fluid to compress the bubble from equilibrium to its minimum volume:

$$\phi_{\mathtt{p,max}} = -\int_{V_0}^{V_{\mathtt{min}}} (p_R - p_0)dV = -\int_{R_0}^{R_0 - R_{\epsilon 0}} (p_R - p_0) 4\pi r^2 dr, \tag{2.24}$$

where p_R is the pressure in the gas bubble with radius R, and p_0 is the pressure at equilibrium, $R = R_0$. Assuming adiabatic conditions (pV^γ = constant), with γ the adiabatic constant in air, gives:

$$p_0 - p_R = \frac{3\gamma R_\epsilon p_0}{R_0}, \tag{2.25}$$

where $R_\epsilon = R - R_0$. Substituting back in equation 2.24 gives in first order approximation:

$$\phi_{\mathtt{p,max}} = 6\pi\gamma p_0 R_0 R_{\epsilon 0}^2. \tag{2.26}$$

Now equating the relations 2.26 and 2.23 gives an expression for the resonance frequency of the air bubble:

$$f_0 = \frac{\omega_0}{2\pi} = \frac{1}{2\pi R_0}\sqrt{\frac{3\gamma p_0}{\rho}}, \tag{2.27}$$

which under normal conditions (atmospheric pressure, room temperature) gives:

$$f_0 R_0 \approx 3.3\,. \tag{2.28}$$

This resonance frequency is called the Minnaert frequency, after Marcel Minnaert who first derived these expressions for adiabatic conditions. In this derivation no attention is paid to surface tension, viscosity and thermal effects. However, for a large range of bubbles ($> 10\,\mu\mathtt{m}$) it provides an accurate approximation.

2.2.2 The Freely Oscillating Bubble

The starting point to obtain an expression for the pressure radiated by the bubble at a distance r from the bubble center is Euler's equation with spherical symmetry:

$$\frac{1}{\rho}\frac{\partial p}{\partial r} = -\frac{\partial v}{\partial t} - v\frac{\partial v}{\partial r}, \tag{2.29}$$

where p is the pressure in the liquid surrounding the bubble, and v is the fluid velocity. The relation between the pressure at a distance r from the bubble center and the instantaneous bubble radius R can be found by integration:

$$\frac{1}{\rho}\int_r^\infty \frac{\partial p}{\partial r}dr = -\frac{\partial}{\partial t}\int_r^\infty v\,dr - \int_r^\infty v\frac{\partial v}{\partial r}dr. \tag{2.30}$$

Again using the velocity profile given by equation 2.22 the following relation is found:

$$\frac{p(r,t) - p_\infty}{\rho} = \frac{R}{r}(\ddot{R}R + 2\dot{R}^2) - \left(\frac{R}{r}\right)^4 \frac{\dot{R}^2}{2}. \tag{2.31}$$

The first term decays in a monopole fashion and represents a spherical wave. It consists of two contributions, the acoustic pressure of the gas inside the bubble and the dynamics of the bubble wall. The second term is solely a contribution of the wall dynamics, and this term is only significant (r^{-4} decay) close to the bubble, which means that it can be neglected in the far field ($r \sim cm$), where the observation usually takes place.

2.2.3 Equation of Motion for Forced Oscillations

To find an equation of motion for the bubble wall, the starting point is again Euler's equation 2.29, or in integrated form, Bernoulli's equation for instationary flow:

$$p + \rho\left(\frac{\partial\Phi}{\partial t} + \frac{v^2}{2}\right) = \texttt{constant}, \tag{2.32}$$

where Φ is the velocity potential, $\vec{v} = \vec{\nabla}\Phi$. In fact this equation is equivalent to equation 2.30, and so evaluation of equation 2.31 just outside the bubble wall ($r = R$) gives:

$$\frac{p_L - p_\infty}{\rho} = \ddot{R}R + \frac{3}{2}\dot{R}^2, \tag{2.33}$$

where p_L is the pressure in the fluid just outside the bubble wall. In [17] it is shown also that:

$$p_L = p_g + p_v - p_\sigma, \tag{2.34}$$

where p_g is the pressure of the gas inside the gas bubble, p_v is the vapour pressure of the fluid in the gas bubble, and p_σ is the surface tension pressure of the fluid. It is also shown that the surface tension p_σ is equal to $2\sigma/R$, and that the gas pressure p_g is equal to:

$$p_g = (p_0 + \frac{2\sigma}{R_0} - p_v)\left(\frac{R_0}{R}\right)^{3\kappa}, \tag{2.35}$$

assuming the gas behaves polytropically with polytropic constant κ. Finally for the pressure in the far field a sinusoidal driving pressure is taken, superimposed on the atmospheric pressure: $p_\infty = p_0 + p_A\sin(\omega t)$. Substituting these expressions in equation 2.33 yields:

$$\frac{3}{2}\dot{R}^2 + \ddot{R}R = \frac{1}{\rho}P(t) \tag{2.36}$$

$$P(t) = \left[(p_0 + \frac{2\sigma}{R_0} - p_v)\left(\frac{R_0}{R}\right)^{3\kappa} + p_v - \frac{2\sigma}{R} - p_0 - p_A\sin(\omega t)\right]. \tag{2.37}$$

Damping

In equation 2.37 no damping terms have been included. The motion of the bubble wall will be damped due to viscosity of the surrounding liquid, due to thermal relaxation of the gas inside the bubble and due to acoustic radiation. Viscosity and thermal damping can be included by adding a term $-4\eta_{\texttt{eff}}\dot{R}/R$ to equation 2.37, where $\eta_{\texttt{eff}}$ is the effective dynamic viscosity. The thermal relaxation can be expressed as a viscosity by:

$$\eta_{\texttt{TH}} = \frac{3p_0}{4\omega}\Im\left(\frac{1}{F}\right), \tag{2.38}$$

where F is the thermal diffusion function, defined as

$$F = \frac{1}{\gamma}\left(1 + \frac{3(\gamma-1)}{Y^2}[Y\coth(Y) - 1]\right). \tag{2.39}$$

Here Y is the ratio between the bubble radius and the thermal diffusion length:

$$Y = \frac{1+i}{2}\frac{R}{L_{\mathtt{D}}} \tag{2.40}$$

$$L_{\mathtt{D}} = \sqrt{\frac{K_g}{2\omega\rho_{\mathtt{g}}C_p}}, \tag{2.41}$$

where K_g is the thermal conductivity constant, $\rho_{\mathtt{g}}$ is the density of the gas, and C_p is the heat capacity of the gas at constant pressure. ω Can either be taken as the pulse angular frequency or the resonance frequency of the bubble. κ can be found from:

$$\kappa = \Re\left(\frac{1}{F}\right). \tag{2.42}$$

And $\eta_{\mathtt{eff}}$ now becomes:

$$\eta_{\mathtt{eff}} = \eta_{\mathtt{TH}} + \eta_{\mathtt{liquid}} = \frac{3p_0}{4\omega}\Im\left(\frac{1}{F}\right) + \eta_{\mathtt{liquid}}. \tag{2.43}$$

The compressibility of the fluid, which leads to acoustic radiation, can be modeled in several ways, the simplest one being the addition of a term $R/c\ \partial P(t)/\partial t$ to equation 2.36. The modified Rayleigh-Plesset equation now becomes:

$$\frac{3}{2}\dot{R}^2 + \ddot{R}R = \frac{1}{\rho}\left(P(t) + \frac{R}{c}\frac{\partial P(t)}{\partial t}\right) \tag{2.44}$$

$$P(t) = \left((p_0 + \frac{2\sigma}{R_0} - p_v)\left(\frac{R_0}{R}\right)^{3\kappa} + p_v - \frac{2\sigma}{R} - p_0 - p_A\sin(\omega t) - \frac{4\eta_{\mathtt{eff}}\dot{R}}{R}\right). \tag{2.45}$$

2.3 Transcranial Doppler Echography

2.3.1 The Doppler Effect

The definition of the Doppler effect is a change in the observed frequency of a given wave due to relative motion of the source and observer. This is shown in figure 2.5. The change in frequency (f_r) due to movement of the *observer* is given by:

$$f_r = f_t\frac{c+v}{c}, \tag{2.46}$$

where f_t is the original frequency and v is the velocity of the observer. In general the velocity of motion does not have to be in the same direction as the direction of propagation of the wave. If there is an angle θ between the two, equation 2.46 becomes:

$$f_r = f_t\frac{c+v\cos\theta}{c}. \tag{2.47}$$

If not the observer but the source is moving with a certain velocity v, the observed frequency is given by:

$$f_r = f_t\frac{c}{c-v\cos\theta}. \tag{2.48}$$

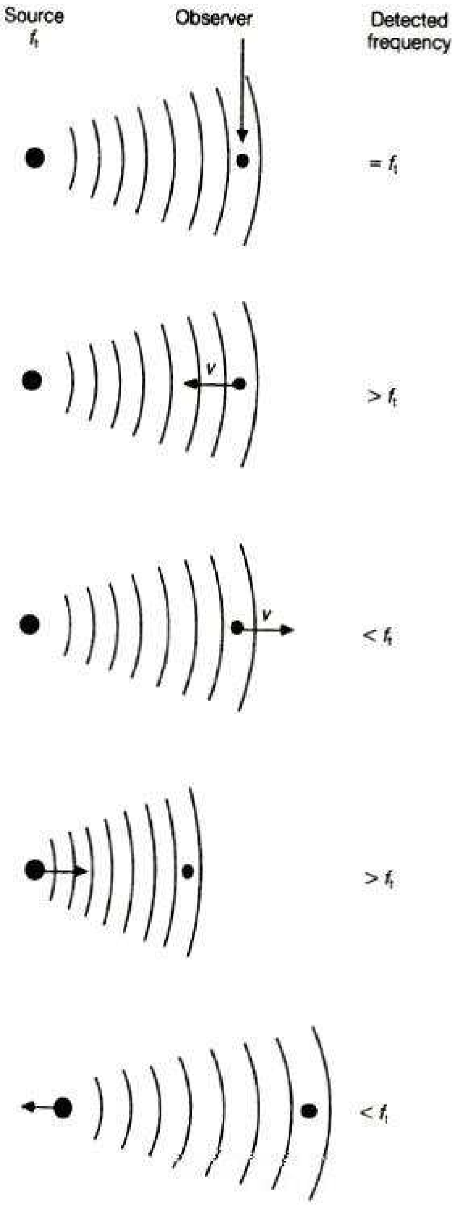

Figure 2.5: The Doppler effect due to motion of source or observer [4].

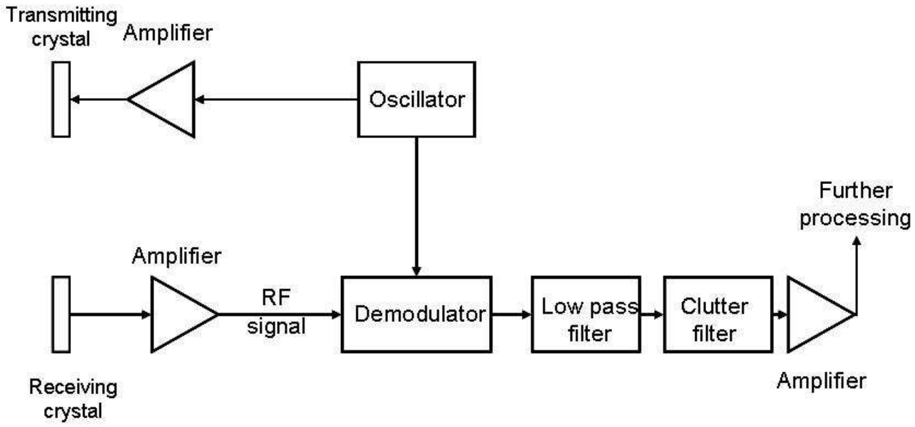

Figure 2.6: Block diagram of CW Doppler operation.

In medical applications, for instance when detecting emboli, both effects occur, since the moving embolus is "observer" and "source" at the same time. The resulting frequency will be in this case:

$$f_r = f_t \frac{c + v\cos\theta}{c} \cdot \frac{c}{c - v\cos\theta} = f_t \frac{c + v\cos\theta}{c - v\cos\theta}. \tag{2.49}$$

The Doppler shift f_d $(= f_r - f_t)$ will therefore be:

$$f_d = f_t \left(\frac{c + v\cos\theta}{c - v\cos\theta} - 1 \right), \tag{2.50}$$

and, when $v \ll c$,

$$f_d = \frac{2 f_t v \cos\theta}{c}. \tag{2.51}$$

For typical particle velocities of 0.5 ms^{-1} with an ultrasound frequency of 2 MHz, the Doppler shift is around 1 kHz.

2.3.2 Continuous and Pulsed Doppler systems

Continuous Wave Doppler

Continuous Wave (CW) Doppler systems are the most simple systems. The basic operation is shown in a block-diagram in figure 2.6. A master oscillator sends a 2 MHz signal through an amplifier to the transmitting crystal. The backscattered signal is received by a receiver and also amplified. Next, the received signal is mixed with the original signal and demodulated. If the transmitted signal will be of the form: $A_t \cos(\omega_0 t)$, then the received signal will have the form: $A_r \cos[(\omega_0 + \omega_d)t + \phi]$. Multiplication with the transmitted signal gives:

$$s(t) = \frac{1}{2} A_r A_t \cos(\omega_d t + \phi) + A_r A_t \cos([2\omega_0 + \omega_d]t + \phi). \tag{2.52}$$

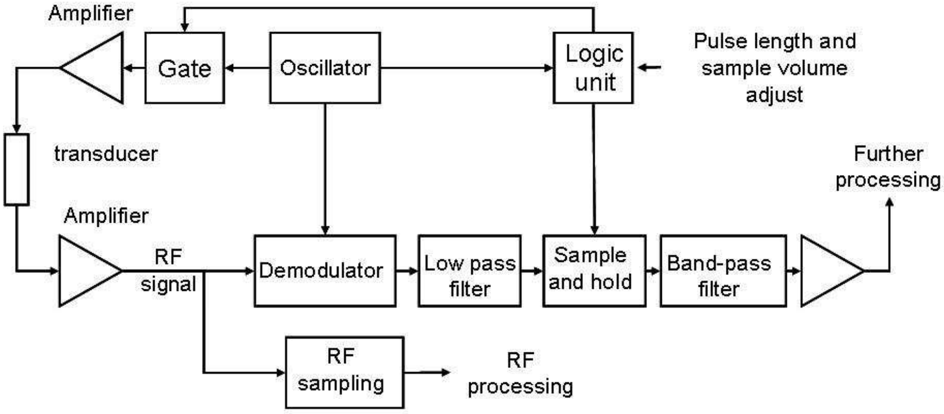

Figure 2.7: Block diagram of PW Doppler system.

After low-pass filtering of this signal the Doppler (audiofrequency) signal will be left, and after high pass "clutter" filtering this can be used for velocity calculations and human observation. The purpose of clutter filtering will be shown later on.

Pulsed Wave Doppler

Pulsed Wave (PW) Doppler Systems are more sophisticated. The most important disadvantage of CW Doppler is that there is no depth information, and thus it is only useful in superficial vessels, when the only interest would be to see whether or not there is flow present in the blood vessel of consideration. PW systems, however, send short ($\sim 10\ \mu s$) pulses, with a certain repetition frequency (f_{rep}). The basic operation of PW systems is shown in figure 2.7. The operation is similar to that of CW systems, however, an additional logic unit is present to control the gate. The signal from the master oscillator is multiplied by the gate signal (approximated by a gaussian pulse), and the returned echo is again mixed with the original signal and low-pass filtered. This signal is fed to a receiver gate, to allow only the signal at a certain delay (i.e. coming from a certain depth).

The sample volume (SV) is the part of the brain that is probed with ultrasound. Its position and dimensions are dependent on the pulse length (t_p), the time delay between pulse transmission and opening of the receiver gate (t_d), and the effective length of the filters preceding the sample and hold (t_g). The position of the start of the sample volume, referenced to the position of the transducer is:

$$x_1 = \frac{c\,(t_d - t_p)}{2}, \tag{2.53}$$

where c is the ultrasound velocity in soft tissue. The end of the sample volume is given by:

$$x_2 = \frac{c\,(t_d + t_g)}{2}, \tag{2.54}$$

therefore the length of the sample volume is given by:

$$\Delta x = x_2 - x_1 = \frac{c\,(t_p + t_g)}{2}. \tag{2.55}$$

The shape of the sample volume (equivalent to the axial sensitivity) depends on the shape of both the transmitted pulse and the receiver gate function. In a simple case it is just the convolution of the transmitted pulse and the impulse response of the filter.

One drawback of PW Doppler systems is that there is a limit to the maximum velocity that can be measured. This is because the Doppler system uses the phase difference between each successive returning ultrasound pulse and a reference signal to extract the Doppler frequency. This can be seen as follows: Suppose a reference time t_0 is chosen, so that the phase of the returning ultrasound pulse is zero at that time: $\phi_0 = 0$ (actually this choice is arbitrary, but for convenience it is chosen to be zero here). Then the next returning pulse has a different phase at the reference time, depending on the time difference $\Delta t^{'}$ between the arrival of the 2 pulses:

$$\Delta t^{'} = 2\frac{x(t) - x_0}{c} = 2\frac{(x_0 - v\Delta t) - x_0}{c} = -2\frac{v\Delta t}{c}, \tag{2.56}$$

where x is the distance from the transducer to the reflector (embolus) and Δt is the time interval between two subsequent ultrasound pulses ($= 1/f_{rep}$). The phase difference is given by:

$$\phi = \phi_0 - 2\pi f_t \Delta t^{'} = \phi_0 + 4\pi f_t \Delta t \frac{v}{c}. \tag{2.57}$$

Now the Doppler shift frequency can be found as the derivative of the phase with respect to Δt:

$$f_d = \frac{1}{2\pi}\frac{\partial \phi}{\partial \Delta t} = \frac{2 f_t v}{c}, \tag{2.58}$$

which is the same expression as equation 2.51 assuming $\theta = 0$.

Since the determination of the corresponding velocity from the phase difference is based on amplitude, this phase difference $(\phi - \phi_0)$ cannot be more than π:

$$\Delta\phi = 4\pi f_t \Delta t \frac{v}{c} < \pi. \tag{2.59}$$

This means that the maximum detectable velocity is:

$$v_{\mathtt{max}} = \frac{c}{4 f_t \Delta t} = \frac{f_{rep} \cdot c}{4 f_t}. \tag{2.60}$$

This limit can also be regarded as just a form of the Nyquist sampling theorem. The minimal frequency of sampling should be twice the maximum frequency in the signal to sample. In this case this maximum frequency is the Doppler shift frequency corresponding to the maximum velocity, and the sampling frequency equals f_{rep}:

$$f_{rep} > 2 f_d. \tag{2.61}$$

Substituting this inequality in equation 2.51 and some rewriting yields:

$$v_{\mathtt{max}} = \frac{f_{rep} \cdot c}{4 f_t \cos\theta}, \tag{2.62}$$

which is equal to the maximum velocity found before, assuming again that $\theta = 0$.
Two ways of enlarging the range of velocities that can be detected, are lowering the ultrasound frequency (f_t) or increasing the pulse repetition frequency (f_{rep}). The former method gives some problems with respect to the transducers used, the latter is limited by the intended depth of the sample volume. For an unambiguous measurement the echo from the end of the sample volume should arrive before the next pulse is transmitted:

$$f_{rep} < \frac{c}{2x}, \tag{2.63}$$

where x is the depth of the sample volume. In a typical measurement, the blood velocity in the Middle Cerebral Artery (MCA) is between $10 - 100$ cm s^{-1} and the MCA is located around 5 cm deep in the head. For the lower limit this means:

$$f_{rep} > \frac{4vf_t}{c} \approx 5\,\mathtt{kHz}, \tag{2.64}$$

and for the upper limit:

$$f_{rep} < \frac{c}{2x} \approx 15\,\mathtt{kHz}. \tag{2.65}$$

For practical reasons f_{rep} is chosen close to the lower limit, although sometimes a higher pulse repetition frequency is desirable. This will be elaborated in the next chapter.

Chapter 3

Materials and methods

3.1 Clinical data

Clinical data about emboli can be obtained from different sources. Gaseous emboli can be obtained from Persistent Foramen Ovale (PFO) trials, in which patients who suffered a stroke at young age are injected with small, coated air bubbles. In healthy people these bubbles are filtered out by the lungs, but in people with this PFO condition the bubbles can travel directly from the right ventricle to the left ventricle. From there they enter the aorta and can be observed in the brain using TCD.

Solid emboli can be obtained by monitoring patients who underwent Carotid Endartectomi (CEA) surgery, for three hours after their surgery. After the carotid artery has been closed, still some plaque residue can be present sticking to the vessel wall, and can enter the blood stream when detached from the wall. These solid particles can also be observed using TCD.

Furthermore emboli can be obtained during cardiac valve repair or replacement surgery. During these procedures the aorta is cross-clamped, and when this clamp is released there can be a shower of air emboli. However, there can be solid particles present too.

3.1.1 Data acquisition

A regular Doppler unit (Pioneer TC8080, Nicolet Biomedical, Hongkong, or Multidop X 4, DWL, Sipplingen, Germany) was used to send 2 MHz ultrasound pulses and to acquire the Doppler (audio)signal. The RF signal, internal clock and PRF trigger were made available, and connected to a 12-bit AD converter of the acquisition computer. Those signals were continuously fed to the ADC, with a sampling frequency (f_s) of 8 or 16 MHz, depending on the Doppler unit used, and stored into a buffer able to contain approximately 3 seconds of the signal. When an embolus is detected by observing the Doppler audio signal, the contents of the buffer are stored on the hard drive by pushing a button. The data is now in an $m \times n$ matrix, each row (m) containing the returned echo of one pulse, where m and n are:

$$m = t \cdot f_{rep} \tag{3.1}$$

$$n = \frac{2\Delta d\, f_s}{c} \tag{3.2}$$

where t is the length in seconds of the acquisition, and Δd is the width of the acquisition window in [m]. Typically f_{rep} is chosen around 5 kHz, and the width of the acquisition window is around 30 mm, 15 mm on either side of the depth setting on the TCD device. In figure 3.1

it can be seen why the PRF is usually chosen close to the lower limit. When a higher PRF is used, correct capturing of the signal becomes difficult, which could lead to sudden "jumps" in the signal, appearing as the discontinuity around a depth of 42 mm. The part of the matrix above the line at 42 mm should be located at the bottom of the plot. This happens because the data input rate exceeds the maximum data throughput rate of the data buffer. It will be shown later on how the amplitude plot is made from the unprocessed matrix.

The sample volume setting of the Doppler unit was chosen as low as possible, maintaining a reasonable signal intensity, to achieve a high depth resolution. For the majority of the measurements this setting was chosen to be 1.1 mm, which corresponds to an ultrasound burst of approximately 4 μs (see figure 3.2). The effective duration of a pulse is defined as twice the root of the mean squared deviation from the time where the pulse reaches its maximum value. For this pulse that value is approximately 1.8 μs. The expression in effective duration is helpful when discussing the bandwidth of the signals under investigation.

In Matlab (©the MathWorks) the matrix is transposed to conform to the standard in literature, so that when plotting the slow time dimension is along the x-axis (m pixels), and the depth dimension is along the y-axis (n pixels). Now each column (depth or fast-time dimension), is high-pass filtered using a fourth order Butterworth filter with a cut-off frequency of 500 kHz, to eliminate any DC components caused by the ADC. Then the signal envelope is obtained using a Hilbert transformation of each column (convolution with $1/(\pi t)$): $S[n] = |s[n] + i\tilde{s}[n]|$ where $S[n]$ is the signal amplitude, and $\tilde{s}[n]$ is the Hilbert transform of the original signal. Now a plot can be made of the amplitude envelope (S), shown in figure 3.3(a). It can be seen that it is difficult to extract information about emboli from this plot, because the embolic signal is overshadowed by the signal from stationary reflections. To suppress this signal each row (slow-time dimension) is high-pass (clutter) filtered again using a fourth order Butterworth filter with a cut-off frequency of 50 Hz (corresponding to a velocity of approximately 2 cm/s). If now an amplitude plot is made an embolus would appear as a region of increased amplitude as seen in figure 3.3(b).

Further Information in RF-data [5]

Under the assumption that the frequency distribution of the ultrasound bursts (and, as a consequence also the envelope of the signal in time) is gaussian (which is a reasonable assumption, see figure 3.2), more parameters can be extracted from the raw RF signals. The spectral power density $G(f)$ can be modeled as:

$$\frac{2(N+S)}{B\sqrt{2\pi}} \exp\left(\frac{-2(f-f_c)^2}{B^2}\right), \tag{3.3}$$

hereby assuming that the signal and noise power (S and N respectively) cover the same rms bandwidth B around the center frequency f_c. This means that the autocorrelated signal as function of time (the inverse Fourier transform of $G(f)$) is:

$$g(t) = \int_{-\infty}^{\infty} G(f) \exp(2\pi i f t)\, df = (N+S) \exp\left(-\frac{1}{2}\pi^2 t^2 B^2\right) \exp(2\pi i f_c t). \tag{3.4}$$

The central frequency follows from the spectral power distribution as:

$$f_c = \frac{1}{A} \int_{-\infty}^{\infty} f |G(f)|^2\, df, \tag{3.5}$$

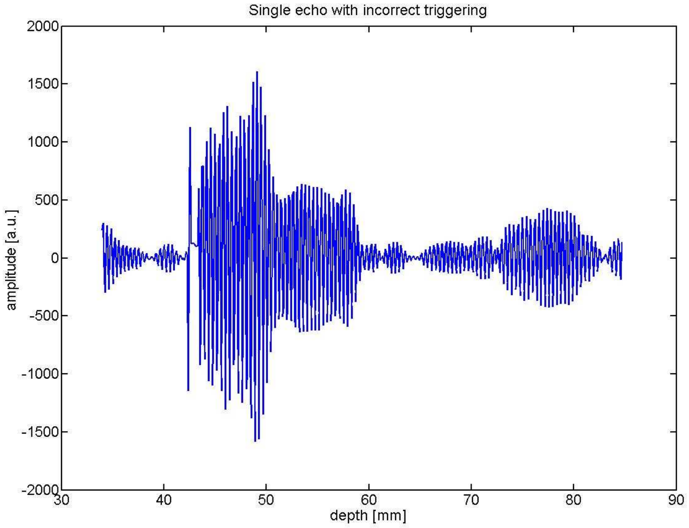

(a) One echo.

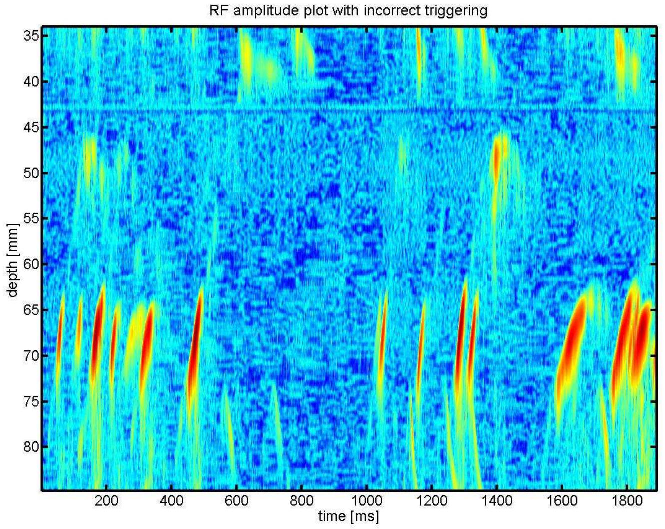

(b) RF matrix.

Figure 3.1: RF matrix and signal with incorrect triggering.

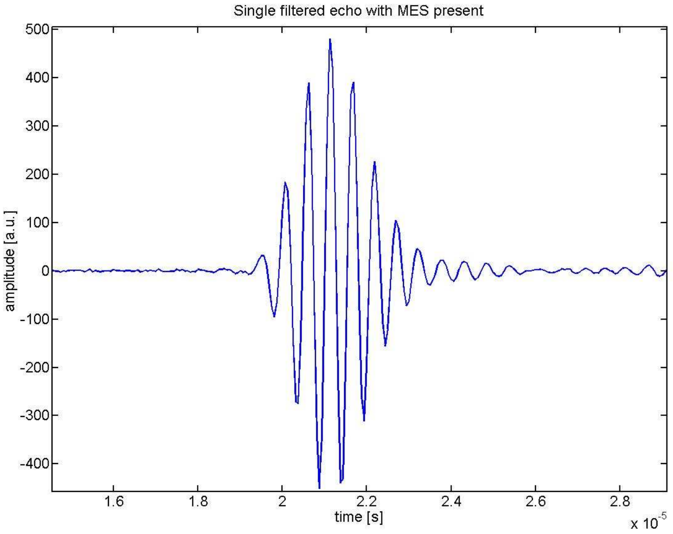

Figure 3.2: Scattered echo of one ultrasound burst.

where A is a normalization constant:

$$A = \int_{-\infty}^{\infty} |G(f)|^2 \, df. \tag{3.6}$$

The bandwidth can be estimated as follows:

$$\sigma_f = \sqrt{\frac{1}{A} \int_{-\infty}^{\infty} (f - f_c)^2 |G(f)|^2 \, df} = \frac{1}{4} B\sqrt{2}. \tag{3.7}$$

The same can be done for the signal as function of time, from which follows:

$$\sigma_t = \frac{1}{2} \frac{\sqrt{2}}{\pi B}. \tag{3.8}$$

From this follows that the product of σ_f and σ_t is equal to $1/(4\pi)$, which is a special case of the localization theorem of Fourier transforms:

$$\sigma_f \sigma_t \geq \frac{1}{4\pi}. \tag{3.9}$$

The Wiener-Khinchin relation states that the cross correlation function $C(\delta, \tau)$ will be the inverse fourier transform of the spectral power density distribution, which is given in equation 3.4. Here τ and δ are the lags of the correlation in time and depth direction, respectively. Taking into account the displacement due to velocity of the scatterers (emboli), the cross correlation function becomes:

$$C(\delta, \tau) = (S + N_\tau) \exp\left(-\frac{1}{2}\pi^2 (\delta + \frac{2v\tau}{c})^2 B^2\right) \exp\left(2\pi i f_c (\delta + \frac{2v\tau}{c})\right), \tag{3.10}$$

where $N_\tau = N$ for $\tau = 0$ and $N_\tau = 0$ for $\tau \neq 0$. Now a change can be made to discrete variables, setting the unit of the depth lag δ to $1/f_s$, the sampling frequency, and the time

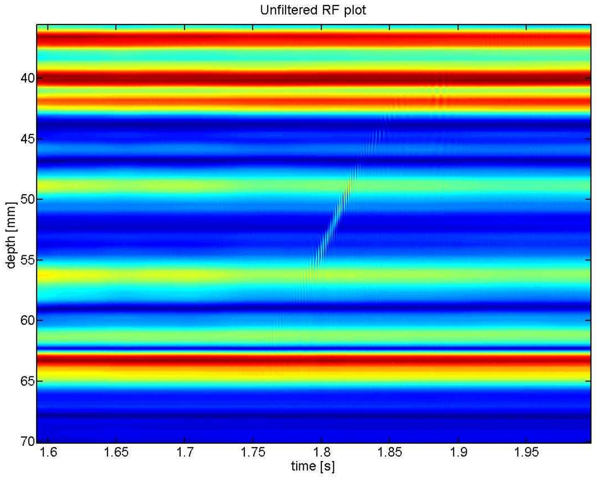

(a) Without clutter filter.

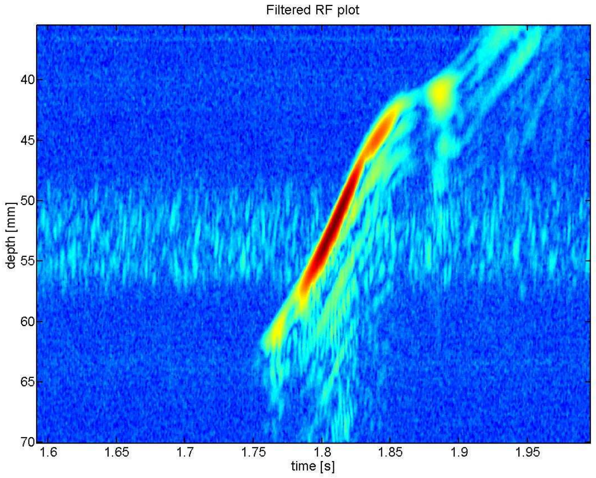

(b) With clutter filter.

Figure 3.3: An embolus in the RF amplitude plot before and after clutter filtering.

lag to $1/f_{rep}$, the pulse repetition frequency. The 4 unknown variables in equation 3.10 $(S/N, B, f_c, v)$ can be solved by evaluating expressions for the cross correlation function for 3 different lags, since it is a complex function:

$$C(0,0) = S + N \tag{3.11}$$

$$C(0,1) = S \exp\left[-\frac{1}{2}\pi^2 \left(\frac{2v}{c\,f_{rep}}\right)^2 B^2\right] \exp\left[2\pi i f_c \left(\frac{2v}{c\,f_{rep}}\right)\right] \tag{3.12}$$

$$C(1,0) = (S+N)\exp\left(-\frac{1}{2}\frac{\pi^2 B^2}{f_s^2}\right)\exp\left(2\pi i \frac{f_c}{f_s}\right). \tag{3.13}$$

This leads to the following expressions for the 4 unknowns:

$$f_c = \frac{f_s}{2\pi}\texttt{arg}(C(1,0)) \tag{3.14}$$

$$v = \frac{c\,f_{rep}}{2f_s}\frac{\texttt{arg}(C(0,1))}{\texttt{arg}(C(1,0))} \tag{3.15}$$

$$B = \frac{\sqrt{2}f_s}{\pi}\sqrt{\ln\frac{C(0,0)}{|C(1,0)|}} \tag{3.16}$$

$$\frac{S}{N} = \frac{|C(0,1)|}{C(0,0)\exp\left(-\frac{1}{2}\pi^2(\frac{2v}{c\,f_{rep}})^2 B^2\right) - |C(0,1)|}. \tag{3.17}$$

The correlation coefficients are obtained from the following formula:

$$C(\delta,\tau) = \frac{\sum_{d=1}^{\texttt{NS}-\delta}\sum_{t=1}^{\texttt{NP}-\tau} r(d,t)r^*(d+\delta,t+\tau)}{(\texttt{NP}-\tau-1)(\texttt{NS}-\delta-1)}. \tag{3.18}$$

3.2 Detection Algorithm

Cowe et al. [7] showed that it is possible to distinguish microembolic signals (MES) in RF intensity plots and create an automated emboli-detection algorithm based on those plots. However, they considered solely single emboli. With the present equipment it is difficult to estimate the amount of emboli in an air-shower. Based on RF signals an effort is made to design an algorithm also capable of counting multiple emboli in a shower. In figure 3.4 this procedure is shown for a single micro-embolic signal (MES).

All local maxima above a certain threshold $T1$ (e.g. 15 dB) and in a certain depth range (e.g. 45–60 mm) are located. A second threshold is defined as $T2$, a certain value V (e.g. 10 dB) below the local maximum. Now a point P1 is defined as the pixel going back in time (to the left in the figure) from the highest local maximum, until a value lower than the second threshold is reached. The same is done for points P2 and P3, in upward direction and to the right, respectively. The slope between points P2 and P1 is determined as slope S. Along this slope S in positive (up) and negative (down) direction from the local maximum two points P4 and P5 are obtained when again a value below $T2$ is reached. A parallelogram can be formed, with height (y(P4)–y(P5)), width (x(P3)–x(P1)), and slope S. All pixels within the parallelogram with an amplitude higher than $T2$ are given the value 0, to indicate that they are part of the event.

The slope between the highest (pixel with lowest depth) and lowest (with largest depth) pixel

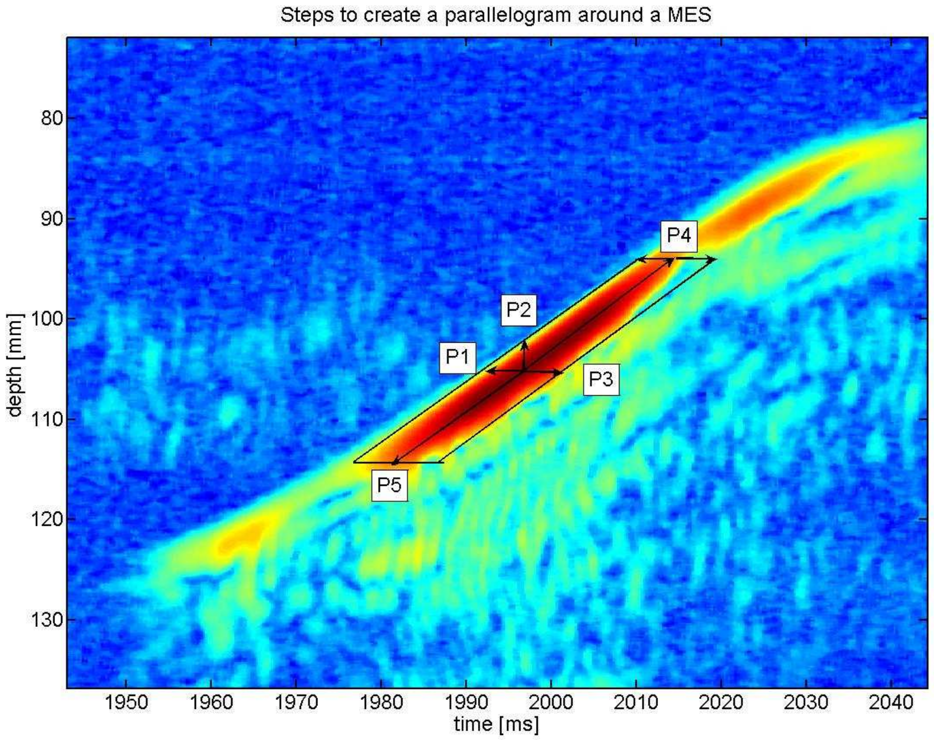

Figure 3.4: Steps to create a parallelogram around a MES.

with zero amplitude as well as the slope between the most right and left pixel with zero amplitude are calculated. The velocity of emboli in the MCA can vary between around 5 and 90 cm/s. These velocity boundaries are transformed (using f_{rep} and sample frequency) into boundaries for the slope(s) of the event. Furthermore the depth range and time range of the event have to be within certain borders, as well as the percentage of zero-value-pixels within the parallelogram. Also some criteria were used to prevent double count of one event. An event is considered to be a MES when all criteria are satisfied. The procedure is repeated for all other local maxima, provided that they were not part of a previous event.

3.3 Simulations

3.3.1 Modeling of the Rayleigh-Plesset equation

Equation 2.44 was solved numerically using the built-in ODE45 differential equation solver in Matlab. In table 3.1 the values for the various parameters in the Rayleigh-Plesset-equation are given. The vapour pressure in the gas bubble is assumed to be negligible. For the driving pulse a 2 MHz sine wave is used, superimposed on a smoothing window. Four windows have been used, a gaussian, Blackman, Hann and Blackman-Harris. The windows are defined as:

$$w(t) = 0.42 + 0.5\cos\left(2\pi\frac{t}{\tau_p}\right) + 0.08\cos\left(4\pi\frac{t}{\tau_p}\right) \qquad |t| < \frac{\tau_p}{2}$$

Table 3.1: Values of parameters used in the Rayleigh Plesset equation.

Parameter	symbol	value	unit
surface tension	σ	0.076	kg $\cdot$ s^{-2}
liquid density	ρ	$1 \cdot 10^3$	kg $\cdot m^{-3}$
sound velocity	c	$1.54{\cdot}10^3$	m/s
thermal conductivity	K_g	$26.2 \cdot 10^{-3}$	W/(m$\cdot K$)
gas density	ρ_g	1.161	kg $\cdot m^{-3}$
heat capacity	C_p	$1.007 \cdot 10^3$	J/(kg $\cdot K$)
blood viscosity	$\eta_{\texttt{blood}}$	$3.8 \cdot 10^{-3}$	kg $\cdot m^{-1} s^{-1}$

$$w(t) = 0 \quad |t| > \frac{\tau_p}{2}, \tag{3.19}$$

for the Blackman window,

$$\begin{aligned} w(t) &= 0.35875 + 0.48829 \cos\left(2\pi \frac{t}{\tau_p}\right) \\ &+0.14128 \cos\left(4\pi \frac{t}{\tau_p}\right) + 0.01168 \cos\left(6\pi \frac{t}{\tau_p}\right) \quad |t| < \frac{\tau_p}{2} \\ w(t) &= 0 \quad |t| > \frac{\tau_p}{2}, \end{aligned} \tag{3.20}$$

for the Blackman-Harris window,

$$\begin{aligned} w(t) &= 0.5(1 - \cos\left(2\pi \frac{(t - \frac{\tau_p}{2})}{\tau_p}\right) \quad |t| < \frac{\tau_p}{2} \\ w(t) &= 0 \quad |t| > \frac{\tau_p}{2}, \end{aligned} \tag{3.21}$$

for the Hann window, and

$$\exp\left(-\frac{1}{2}\left(\frac{at}{\frac{\tau_p}{2}}\right)^2\right), \tag{3.22}$$

for all t, with a taken as 2.5, for the gaussian window. The pulse length (τ_p) and amplitude p_A are varied. The results are shown in the next chapter.

3.4 Flow Phantom Setup

To investigate the possibility to detect small intensity emboli using RF signals a flow phantom has been made, shown schematically in figure 3.5. The set-up consisted of a reservoir, a centrifugal pump providing a stationary flow of 1.5 L/min, an oxygenator (Quadrox BE-HMO 2000, Maquet, Hirrlingen, Germany) and an arterial filter (Terumo). The filter and the oxygenator served to de-gas the porcine blood flowing in the loop. The filter also filtered particles, introduced to mimic particulate emboli, so the set-up could be used to record multiple sessions. The transducer was fixed on the edge of a bowl filled with water, in which

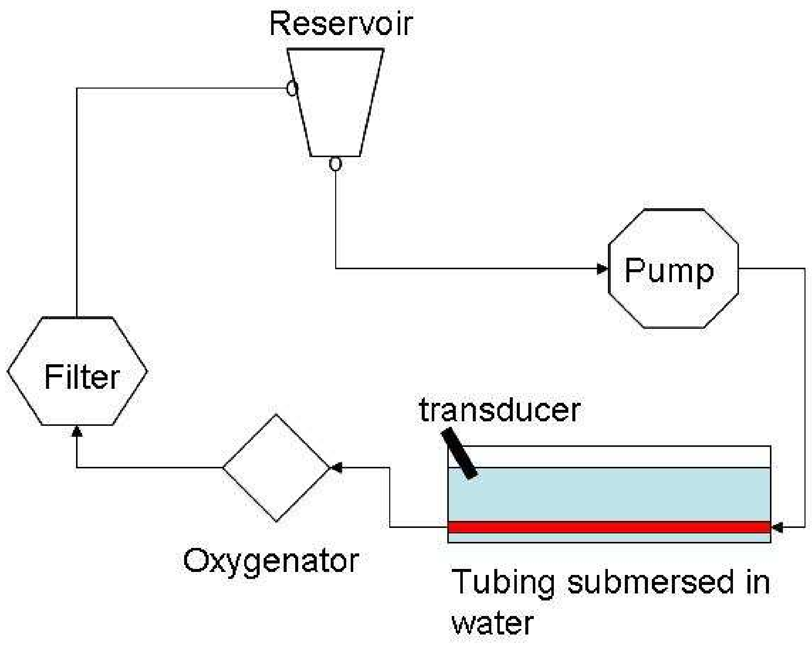

Figure 3.5: Schematic diagram of the flow phantom set-up.

a part of the tubing was submersed. The tube was insonified under an angle of approximately 30 degrees. Small particles of various sizes ($\sim$ 50 micron, $<$ 300 micron, 300–425 micron and $>$ 425 micron) were introduced into the reservoir after the blood has been running for several hours and the blood is almost air-free. The data was acquired in the way described in the first section of this chapter.

Chapter 4

Results and Discussion

4.1 RF Method for Emboli Detection

Mess et al. [21] and Cowe et al. [6] showed in their papers that plotting the clutter filtered RF matrix can be an alternative method to identify emboli. To automate the detection of emboli an intelligent method of shape recognition has to be developed. The shape of micro embolic signals (MES) as they occur in the RF matrix intensity plots, however, depends on many factors. First of all the settings and characteristics of the TCD device influence the appearance. The pulse repetition frequency determines the thickness of the MES in the (slow) time direction, whereas the burst length (or sample volume setting) determines the thickness in depth (or fast-time) direction. The slope of the MES is determined by the sample frequency, f_{rep} and the speed of the embolus. However, even with the same settings, in the same patient, the shape can differ from MES to MES. This is the case especially in measurements in which the Nicolet TCD device was used, see figure 4.1.

The explanation for the differences in shape is not found so easily. One possibility is that there are small variations in the burst length of the ultrasound pulse over time, another possibility is that the intensity of the ultrasound beam is not uniform over the entire beam width, which can lead to shape variations because the embolus does not travel exactly parallel to the beam. Upon closer investigation of one particular MES (figure 4.2) it can be seen that the former explanation is not very probably. For all 4 lines the length of the first half of the burst is around 3.2 μs. However, it appears that for lines 2 and 4 the returned echo is more asymmetric than for lines 1 and 3. Especially the difference between line 3 and 4 is obvious. This rules out a mere intensity effect. In table 4.1 the values for the rms bandwidth in time and frequency are given. The difference between lines 1 and 3, and 2 and 4, respectively is obvious. The frequency bandwidth of lines 1 and 3 is much larger, which indicates a shorter pulse length.

The explanation of the shape variations in this case is most probably a combination of burst length variations, non-uniformity of the ultrasound beam and interaction of the beam with the (gaseous) embolus.

The second factor to influence MES shape is the trajectory of the embolus. As seen in the introduction not only the MCA but also the ACA and PCA can be insonified with TCD. Furthermore, the velocity of the embolus depends on the path traveled through the vessel and on the moment in the cardiac cycle. In figure 4.3 an example is given of MES with different shapes due to different velocities in the same vessel.

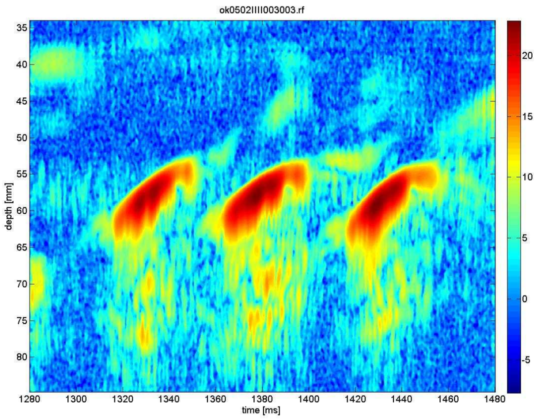

(a) 3 MES with different shapes.

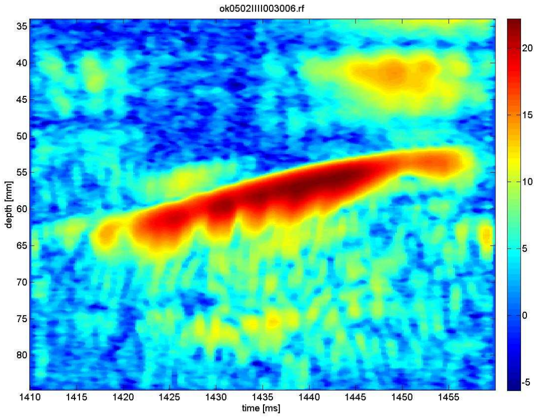

(b) MES with irregular shape.

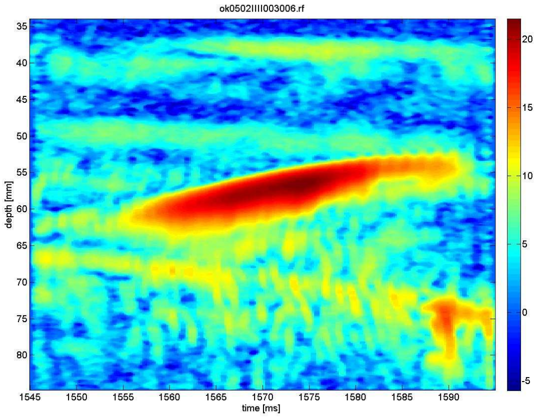

(c) MES with regular shape.

Figure 4.1: Different MES shapes found in the same patient, note the difference between 4.1(b) and 4.1(c).

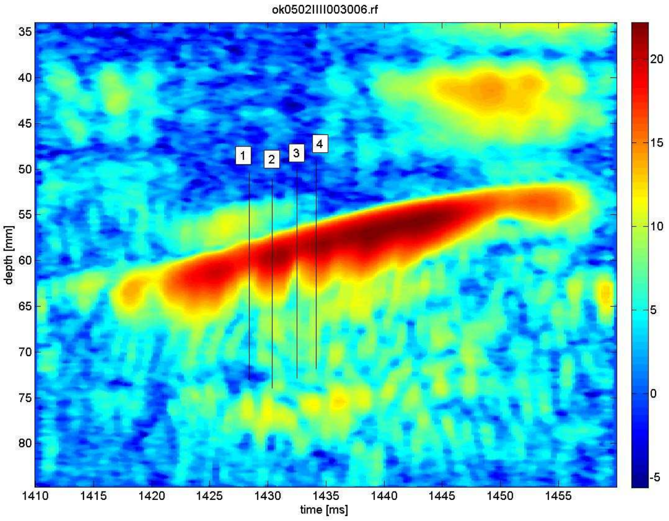

(a) 4 lines.

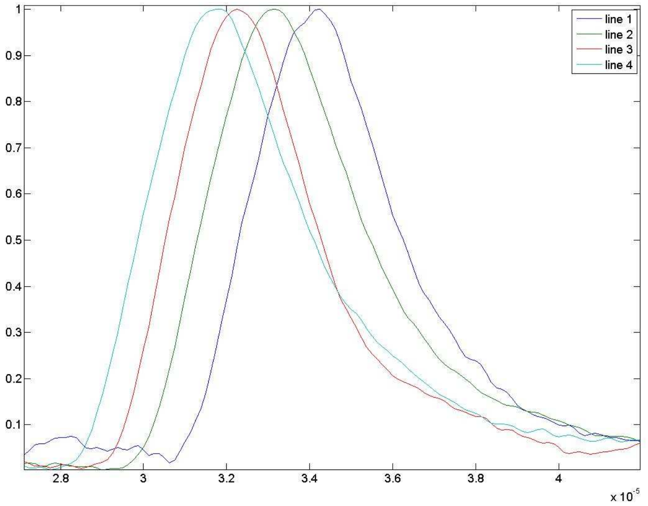

(b) normalized intensity.

Figure 4.2: Normalized intensity of four different (filtered) echoes plotted against depth (fast time direction).

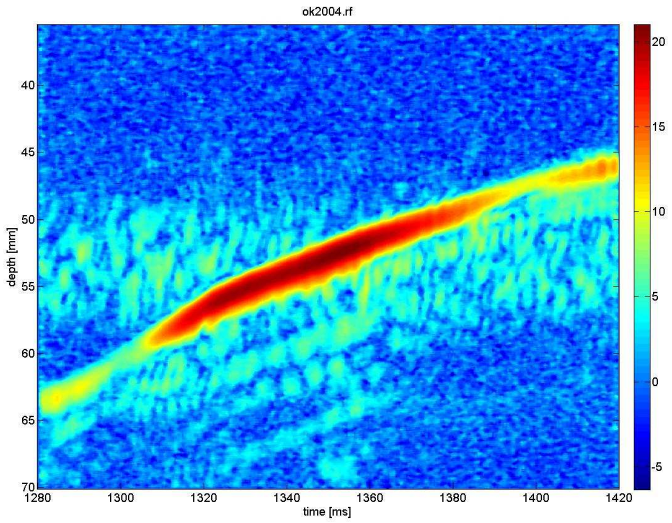

(a) slow embolus.

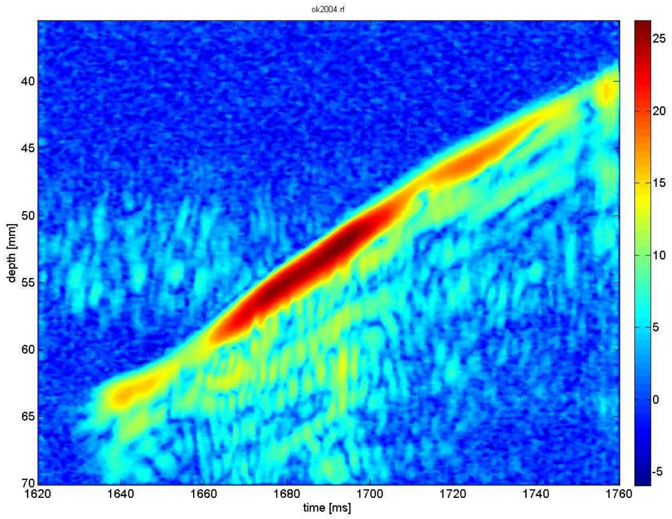

(b) fast embolus.

Figure 4.3: 2 MES with different velocities, the upper MES has a velocity of $\sim$ 12.5 cm/s, the lower one a velocity of $\sim$ 28 cm/s.

Table 4.1: Root mean square bandwidth in time and frequency for four echoes in figure 4.2(a).

Line	bandwidth in time $\cdot 10^{-6}$ s	bandwidth in frequency $\cdot 10^{4}$ Hz	$\sigma_t \cdot \sigma_f$
1	1.59	4.57	0.0724
2	1.75	3.92	0.0684
3	1.48	4.39	0.0652
4	1.83	3.91	0.0715

In some cases it is difficult to assess whether different MES originate from emboli in the same vessel or not. This is especially the case when air-showers occur after cardiac surgery. Some examples can be seen in figure 4.4. In figure 4.4(a) the difference between the three MES is clear. MES 3 has entered a vessel other than the MCA, possibly the anterior cerebral artery (ACA). The difference between MES 1 and 2 arises from a difference in velocity as a consequence of a different trajectory within the vessel or a different moment in the cardiac cycle. The difference in the distal part arises from the fact that the MCA ends in a bi- tri- or even quadrifurcation [20]. In figure 4.4(b) the different shapes cannot be so easily explained. Especially for MES 2 and 3 it cannot be determined directly in which vessel they occurred. One explanation for their shape is that they traveled in a vessel almost perpendicular to the ultrasound beam. Another is that they were traveling not in the center of the MCA but close to the wall, where the blood velocity is much lower. However, the former explanation is more probable, since MES 3 and 4 cross paths. It is very unlikely that two emboli travel in the same vessel at the same time each in different directions. In figure 4.4(c) another shape can be observed. In this case the ultrasound beam only insonated a very proximal part of the MCA, which can be deducted from the shape of MES 1. MES 2 has again a very different shape and probably will have occurred in a small vessel close to the MCA.

4.2 Counting Algorithm

The processed RF matrices are read by 3 independent observers. An event is classified as MES when 2 of the 3 observers agree to classify it as embolic. The local maximum of the event had to be within a certain depth range that changed for every patient. Also the entire event had to be in the matrix. Events cut off by the start or the end of the matrix were ignored. This way each event classified as MES by the algorithm can be classified as true positive (TP) or false positive (FP). A training set of 20 recordings taken from 5 different patients, containing 201 MES upon investigation by 3 observers, was used to obtain the optimal values for the most important algorithm parameters, $T1$ and V. This was done by monitoring sensitivity and positive predictive value (PPV) while varying $T1$ and V. For $T1$ values of 15, 12 and 10 dB were taken, and for V values of 10, 8 and 6 dB. The sensitivity was calculated by

$$S = \frac{\#\,\texttt{TP}}{\#\,\texttt{events}\,\texttt{classified}\,\texttt{as}\,\texttt{MES}}, \tag{4.1}$$

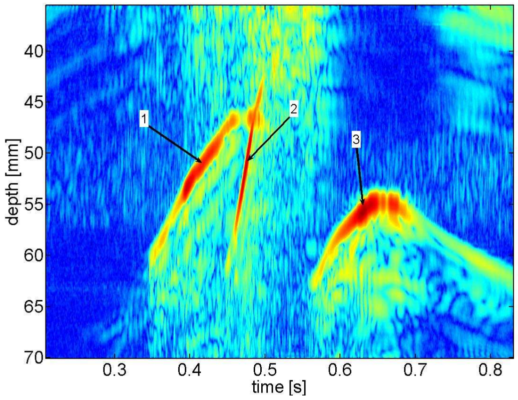

(a) 3 MES with different shapes. MES 1 and 2 occurred in the MCA, MES 3 probably occurred in the ACA.

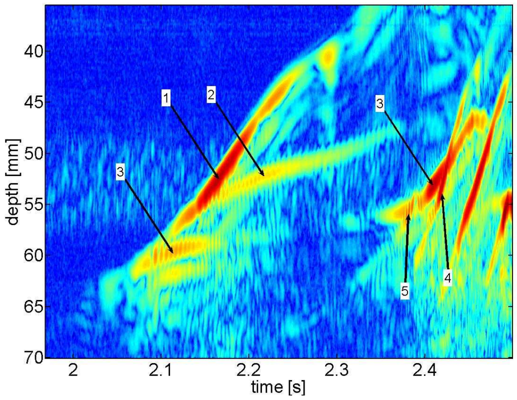

(b) 5 MES probably occurring in different vessels.

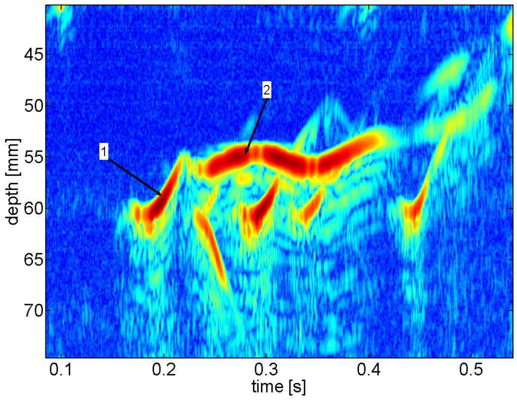

(c) 5 MES in the proximal MCA, 1 MES (2) in an unknown vessel.

Figure 4.4: Parts of 3 different RF amplitude plots showing MES with different shapes due to different trajectories. Figure a and b are taken from the same patient, figure c is taken from a different patient.

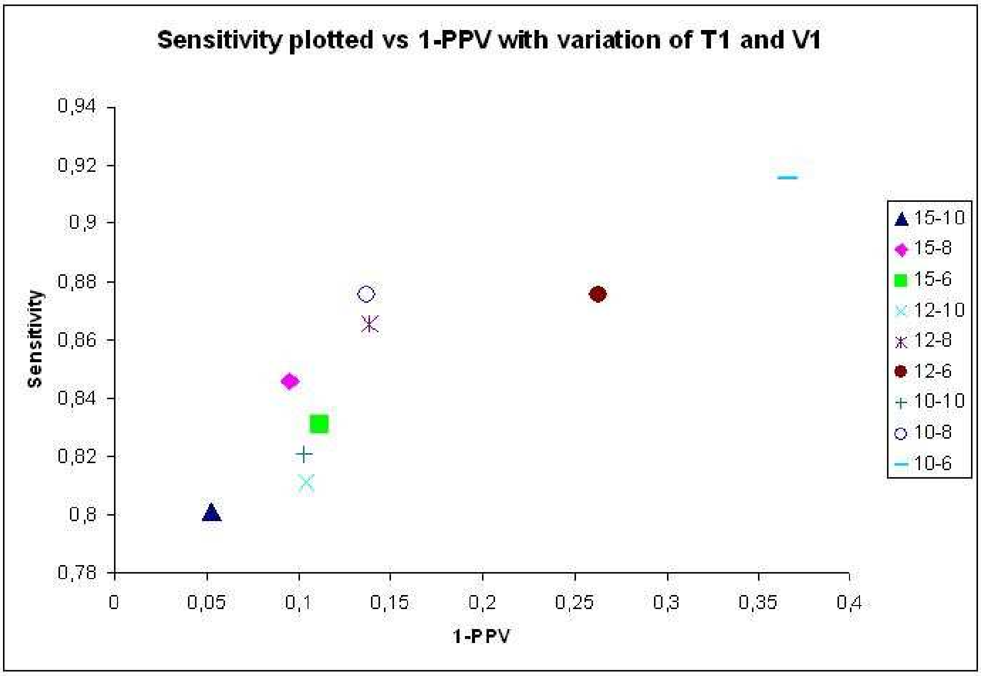

Figure 4.5: Receiver operated characteristic with variation of $T1$ and V (see legend).

and varied between 0.80 for $T1 = 15$ dB and $V = 10$ dB and 0.92 for $T1 = 10$ dB and $V = 6$ dB. The PPV was calculated by

$$\text{PPV} = \frac{\#TP}{\#TP + \#FP}, \tag{4.2}$$

and ranged from 0.63 for $T1 = 10$ dB and $V = 6$ dB to 0.94 for $T1 = 15$ dB and $V = 10$ dB. In general it can be seen that lowering $T1$ and V improves the sensitivity of the algorithm while sacrificing specificity. The receiver operating characteristic (ROC) curve is shown in figure 4.5. The optimum in the ROC is the upper left point in the curve, which in this case corresponds to $T1 = 10$ dB and $V = 8$ dB, with a sensitivity and PPV of 0.88 and 0.86, respectively.

Using these optimal parameters the algorithm is applied to a different set of matrices. This set consists of 21 matrices taken from 4 different patients. A total of 388 MES was found by visual inspection. The number of MES per matrix varied from 3 up to 71. A total of 277 events was classified as MES by the algorithm, which yields a sensitivity of 0.71. Only 12 events were falsely classified as MES, which gives a PPV of 0.96.

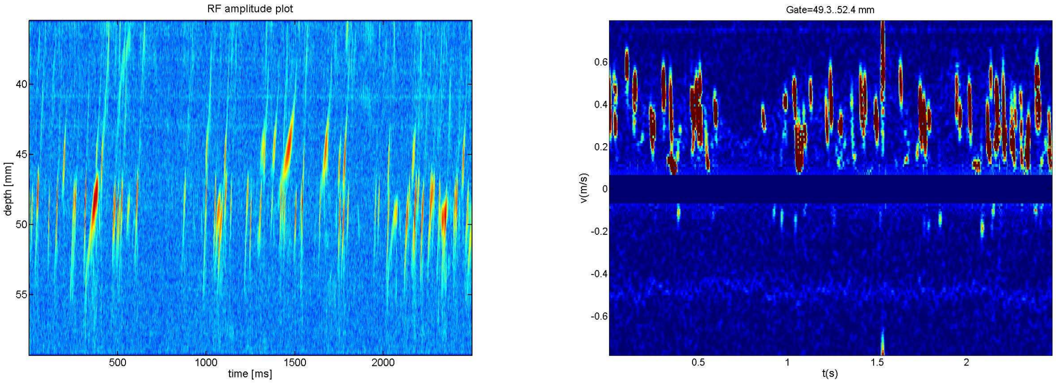

(a) RF plot (b) Doppler velocity spectrum

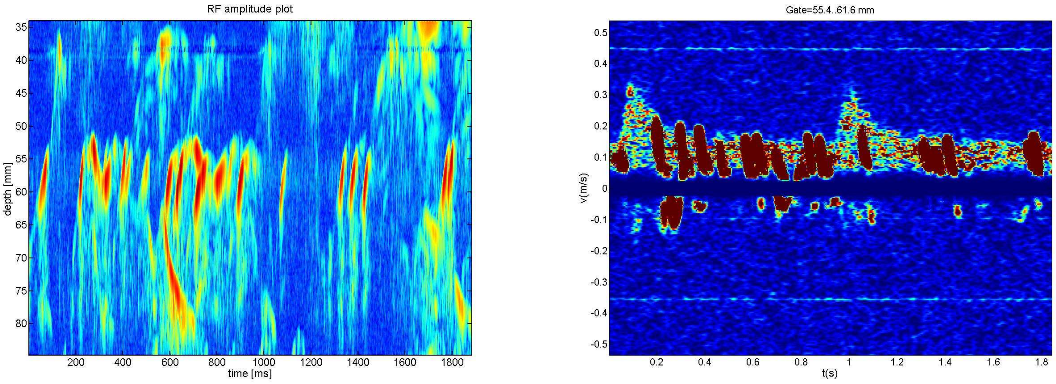

(c) RF plot (d) Doppler velocity spectrum

Figure 4.6: RF amplitude plot and Doppler velocity spectrum of 2 data sets used to test the counting algorithm.

4.2.1 Comparison with Doppler Spectra

The question remains whether or not the method explained here really proves to be better than already existing methods. In figure 4.6 for two matrices the Doppler velocity spectrum as well as the RF amplitude plot are shown. Also in the Doppler plot many MES can be distinguished, but when 2 MES occur at approximately the same time at different depths the RF method is the only one able to distinguish between them. This can be observed in figure 4.7. The part between 1.5 and 1.6 seconds contains 2 MES, where the right part of the first MES occurs at the same time as the left part of the second. In the RF plot the 2 MES can be distinguished clearly, in the Doppler velocity plot they appear as a continuous spot of increased intensity. This is the most important advantage of the RF method, the fact that it is 2 dimensional.

4.2.2 Relation between dB values and Embolus to Blood Ratio (EBR)

In literature the standard way to classify the intensity of MES is the embolus to blood ratio (EBR). The EBR can be found using the demodulated Doppler signal or the RF amplitude

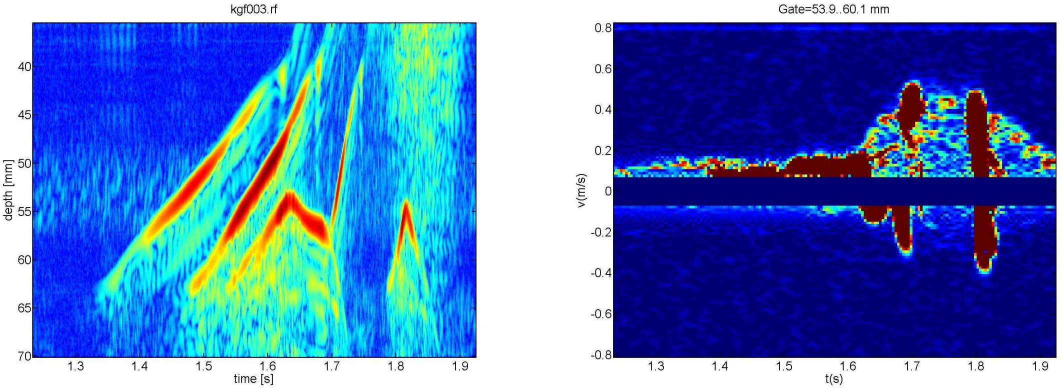

(a) RF plot

(b) Doppler velocity spectrum

Figure 4.7: RF amplitude plot and Doppler velocity spectrum, zoomed in on a part with several MES.

matrix. In the latter case the depth of the blood signal has to be known. For this the method described in 3.1.1 can be used. The signal to noise ratio (SNR) should be more than 1 when blood is present (or any moving objects) and will be less than 1 in other parts of the matrix. This is illustrated in figure 4.8. The EBR is calculated from:

$$\texttt{EBR} = 20\log_{10}\left(\frac{\texttt{rms(with MES)}}{\texttt{rms(without MES)}}\right) \tag{4.3}$$

where the rms values are calculated in a window approximately 40 ms long in time. The depth range of the window depended on the localization of the blood flow. Averaging in depth and time is necessary because of ”speckle” [2]. The backscattered pressure can vary by 6 dB because of interference patterns caused by the backscattering from different packs of red blood cells. Averaging in depth and time cancels this effect in 2 of the three dimensions. In the direction transversal to the ultrasound beam still some variation can be present, depending on the width of the beam. For several MES in 2 patients the calculated EBR value has been plotted against the peak value in the RF amplitude plot. The results are shown in figure 4.9. There appears to be a linear relation between the two values in both patients. The parameter of interest is the EBR value at a peak MES amplitude of 10 dB (the threshold of detection of the algorithm). From a linear fit through the data points, the corresponding EBR value for patient 1 is found to be approximately 2 dB, for patient 2 this value is approximately 6 dB. In literature [9] the inter-observer agreement on MES detection drops drastically below an EBR of 10 dB, which indicates that a peak value threshold of 10 dB is very reasonable.

4.2.3 Most Common Errors

The errors made by the algorithm can be classified as False Positive (FP) or False Negative (FN). An increase in the number of FPs will yield a lower PPV, while an increase in the number of FNs will give a lower sensitivity. Various sources of false negatives were present. When MES were too close together in time to distinguish them, this gave rise to some false negative events (figure 4.10(a)). However, this is a fundamental limit of all methods, since the resolution in time is limited (and related to the pulse repetition frequency). The algorithm

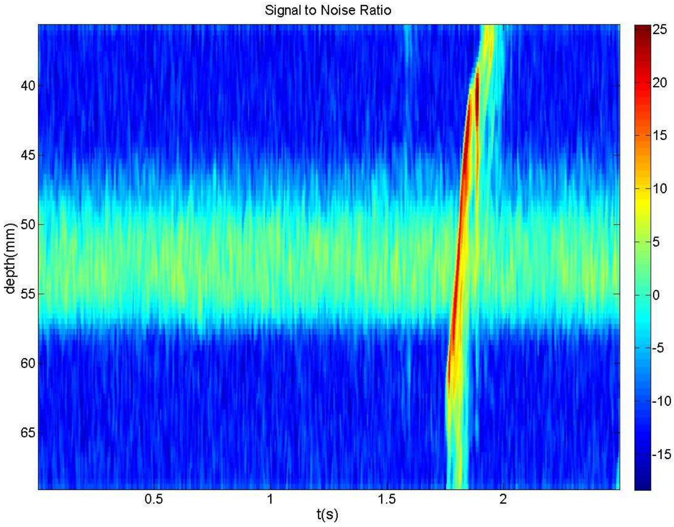

Figure 4.8: Signal to Noise Ratio (SNR) estimation of a data set. Blood is present where the SNR is larger than 0 dB.

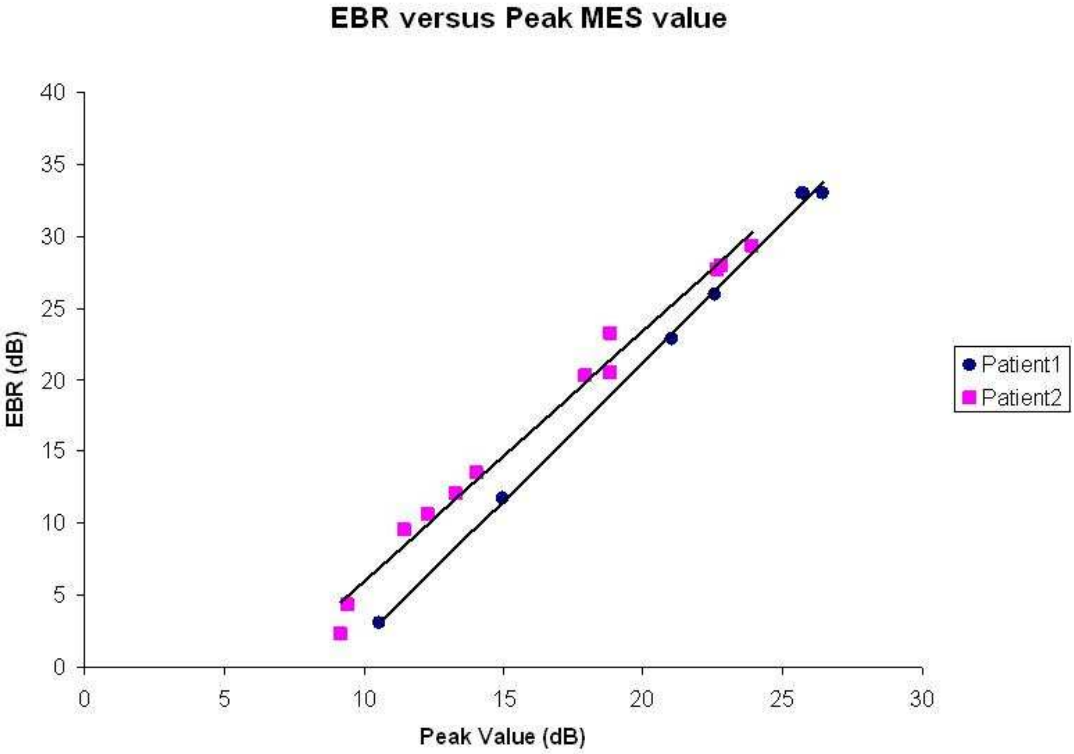

Figure 4.9: Relation between peak embolic amplitude in RF plot and calculated EBR for several MES taken from 2 different patients.

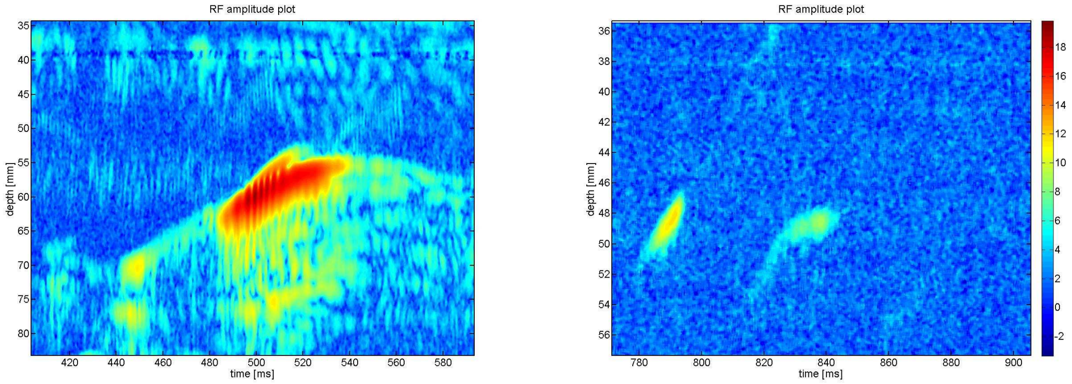

(a) Two MES too close in time to resolve them.

(b) MES with peak amplitude below 10 dB.

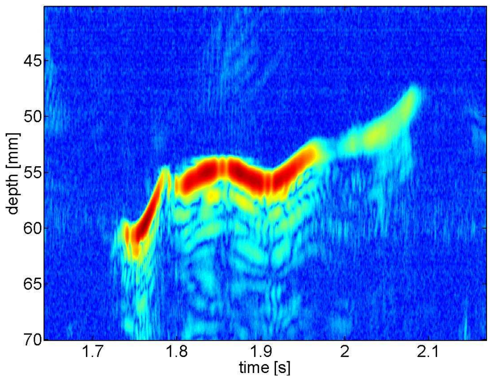

(c) MES with local maximum in downward slope.

Figure 4.10: Three examples of possible false negatives in the RF detection algorithm.

could resolve two MES 10 ms separated, depending on their shape. It is difficult and probably not necessary to improve this resolution. Another source of FNs is the detection threshold. In one patient a significant number of MES had an peak amplitude of less than 10 dB, which made them non-detectable (figure 4.10(b)). However, as seen in the previous section, the 10 dB threshold is not very high. Lowering the threshold means sacrificing specificity and calculation speed. A final source is the occurrence of MES with an inflection point. If in that case the local maximum occurs in the downward part of the MES it is often not classified as MES (figure 4.10(c)). These MES, however, rarely occurred.

The two most important sources of false positives are artifacts and double count of a single MES. Double count can be prevented using a more sophisticated method of placing a contour around an event (figure 4.11(a)). Artifact rejection (figure 4.11(b)) in the algorithm is based mainly on the slope of the event. Also the area of 0-pixels within the parallelogram can function as a criterium. The best method, however, to reject artifacts is to use a velocity plot, which has not yet been included in the algorithm but would not be very difficult to do. In this case also, the method described in 3.1.1 can be used.

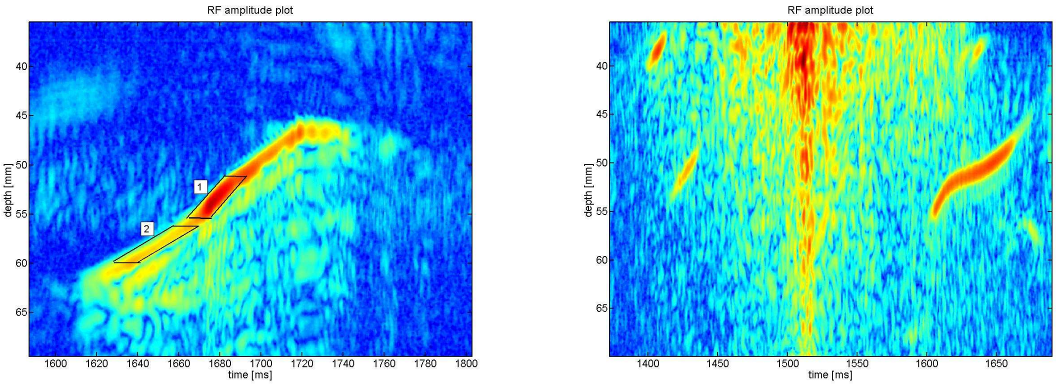

(a) Possible double count of one MES.

(b) Artifact possibly classified as MES.

Figure 4.11: Two examples of possible false positives in the RF detection algorithm.

Velocity estimation

The velocity and signal to noise ratio plot of one data set are shown in figure 4.12. To use the velocity plot, first the velocity of pixels with an SNR lower than 0 dB has to be set to zero. Then the average velocity of all pixels forming an event can be calculated and used to discriminate between artifacts and MES. For this purpose, however, the velocity plot has to be interpolated to the same size as the original RF matrix. Using this approach, in the RF amplitude plot only the various events would have to be separated by placing a contour around them, and the discrimination can be based on the velocity.
The SNR plot can be used as a substitute for the RF amplitude plot, however, the SNR estimation is not accurate for small objects such as emboli. This is because the dimensions of the acquisition window (in time and depth) are always larger than the embolus. This causes the signal strength to be dependent of the position of the embolus in the window. The noise power, however, covers the whole window. The SNR for MES will always be underestimated this way. Furthermore slower emboli will have a relatively higher SNR than faster emboli because they are staying inside of the detection window longer. This can be seen by comparing the RF amplitude plot (c) and SNR plot (b) of a data set containing a 'slow' and a 'fast' MES (figure 4.12). This, however, does not impede the use of the *velocity* plots in improvements of the algorithm described in this work.

4.3 Solid-Gas Discrimination

4.3.1 RF Plots of Solid and Gaseous MES

As stated in the introduction, using traditional Doppler methods it is not easy to distinguish between gaseous and solid emboli. However, in normal RF amplitude plots, those MES do not exhibit specific characteristics to distinguish them from each other either. In figure 4.13 an example of both a solid and gaseous MES is shown. The variations in shape are a consequence of the fact that the two MES were observed in different patients. This means that other methods have to be explored to distinguish them.

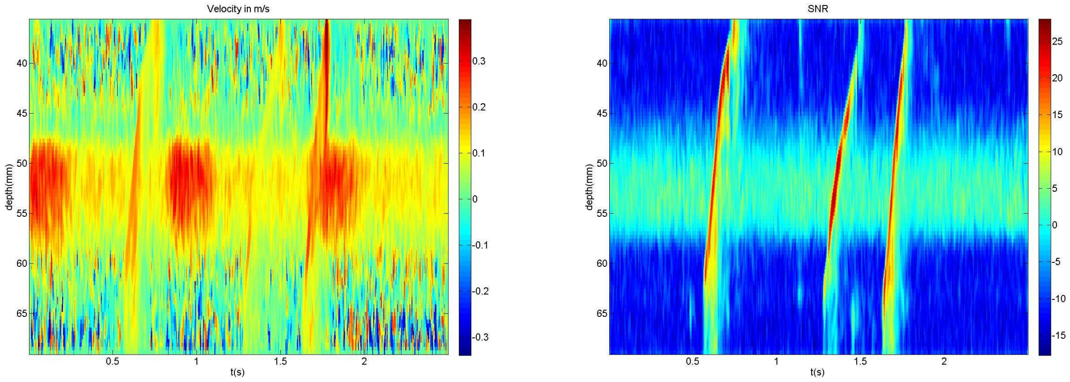

(a) Velocity plot; the values in parts where the signal to noise ratio is too low are not used.

(b) Signal to noise ratio (SNR) distribution

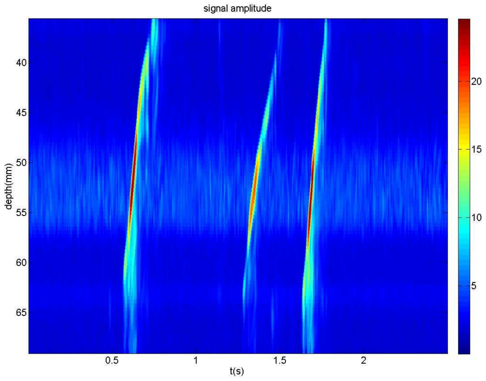

(c) Normal RF amplitude plot, averaged to fit to the dimensions of the velocity and SNR matrices.

Figure 4.12: Velocity, Signal to Noise Ratio (SNR) and RF amplitude plot of one data-set.

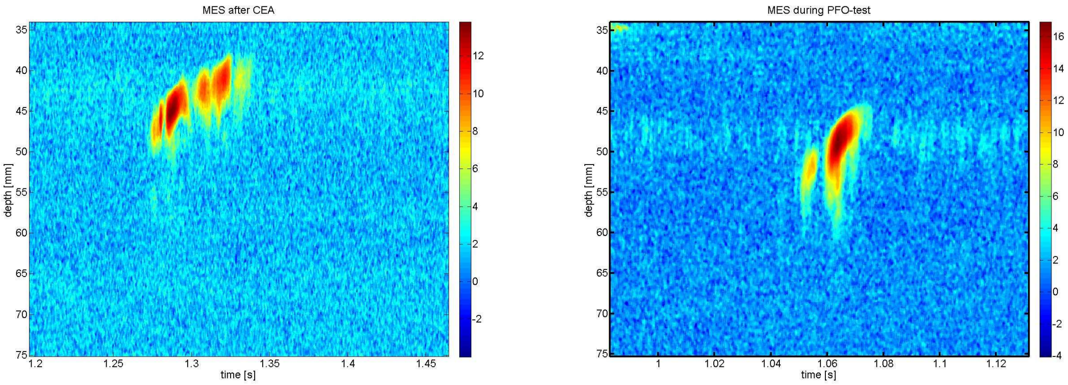

(a) MES obtained after carotid endarterectomy surgery.

(b) MES obtained during 'PFO' test.

Figure 4.13: Examples of one solid and one gaseous MES.

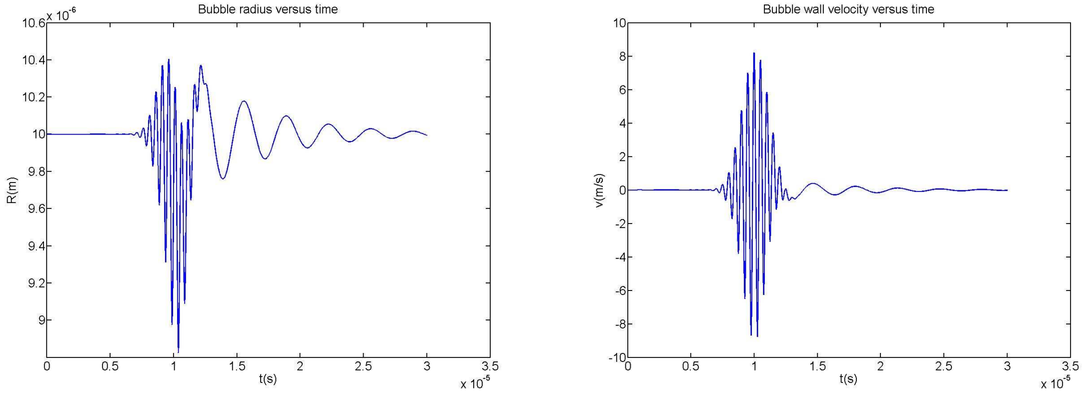

(a) bubble radius. (b) wall velocity.

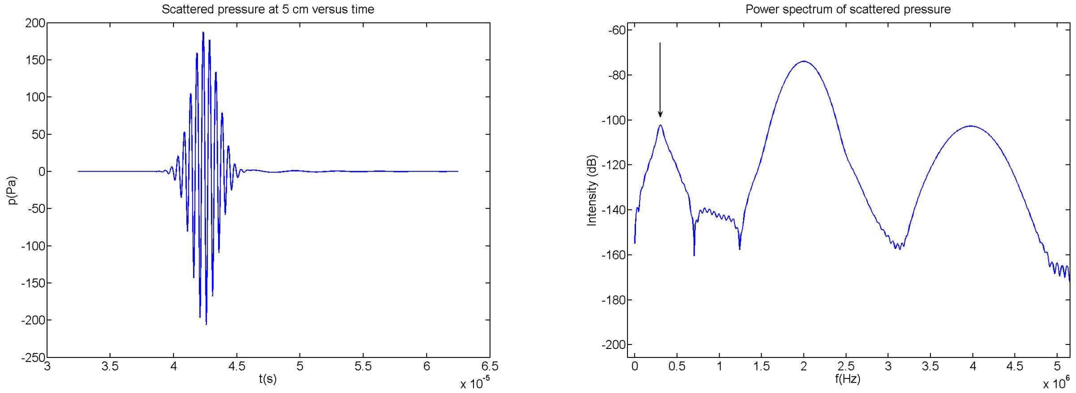

(c) scattered pressure. (d) power spectrum.

Figure 4.14: Bubble radius, wall velocity, and scattered pressure as function of time. The incident pressure pulse had a duration of 5 μs, an amplitude of 1 MPa and a frequency of 2 MHz. The vertical arrow in figure (d) indicates the bubble resonance frequency.

4.3.2 Numerical Simulations

To investigate the behaviour of small air bubbles when insonified by ultrasound the Rayleigh-Plesset equation has been simulated numerically. In figure 4.14 the bubble radius, wall velocity and the scattered pressure at a distance of 5 cm are shown, using a 5 μs, 2 MHz, 1 MPa incident pulse. It can be seen immediately from figure 4.14(a) that after the driving pulse ends ($t = 12.5\,\mu s$) the bubble continues to oscillate at its resonance frequency. This can be observed also in the power spectrum of the scattered pressure (figure 4.14(d)) where an obvious peak is visible around 330 kHz, which is the resonance frequency of a bubble of $10\,\mu m$ radius (equation 2.28). If this effect can be observed acoustically for a range of bubble radii, it can prove to be a reliable method of distinguishing between gaseous and solid emboli, since solid emboli are rigid, incompressible scatterers in which this effect will not occur. Furthermore, this way the standard FDA-approved 2 MHz TCD pulse can be used, and it is not necessary to know the bubble size a priori, provided a broad-band receiver is used.

Influence of Window

The previous example was obtained using a Gaussian window. It can be hypothesized that the amplitude of the effect shown by the simulations will depend on the properties of the window used. To investigate this the simulation has been performed with all four windows described in the previous section. The results can be seen in figure 4.15. The Blackman-Harris window has a slightly smaller duration and larger bandwidth. The influence on the oscillation after the pulse is negligible, the difference is 1 dB or less between the peak powers at the resonance frequency (figure 4.15(f)). This means that for the remaining simulations any of the four windows can be used. In this case a Gaussian window is chosen.

Dependence on Pulse Duration and Acoustic Pressure

To investigate the influence of pulse duration and intensity as well as bubble size, the power of the resonance peak relative to the 2 MHz peak is plotted against bubble radius for various pulse lengths and intensities. This is shown in figure 4.16. In figure 4.17 the same plot is shown, zoomed in on small radii. It can be observed in figure 4.16 that the ratio of the power at the resonance frequency and the power at the insonation frequency increases with decreasing bubble radius (starting from $R = 60\,\mu m$). This is to be expected, since the resonance frequency approaches the insonation frequency with decreasing radius, which will lead to more overlap between the two frequencies and a stronger effect. However, the magnitude of the effect reaches a maximum at a certain radius, followed by a sharp drop towards smaller radii. In figure 4.18 the radius at which the maximum effect occurs ($R_{\mathtt{max}}$) is plotted against insonation power and pulse duration. $R_{\mathtt{max}}$ does not seem to be dependent of the acoustic pressure, but seems to be proportional to the pulse duration.

Also for the apparent anti-resonances the corresponding radii have been plotted against pulse duration and acoustic pressure, see figure 4.19. The radius at which the minimal effect occurs ($R_{\mathtt{min}}$) increases with increasing acoustic pressure as well as with increasing pulse duration.

It is hard to directly relate bubble radii to the other model parameters, but by converting them to their corresponding resonance frequencies, a possible dependence can be found more easily. To this end, equation 2.27 is modified to incorporate viscous effects and surface tension to:

$$f_0 = \frac{1}{2\pi R_0\sqrt{\rho}}\sqrt{3\kappa(p_0 + \frac{2\sigma}{R_0}) - \frac{2\sigma}{R_0} - \frac{4\eta_{\mathtt{eff}}}{\rho R_0^2}} \tag{4.4}$$

where κ and $\eta_{\mathtt{eff}}$ can be found from equations 2.42 and 2.43, respectively (figure 4.20). There does not appear to be any discontinuity or peak in the plots of effective viscosity and polytropic constant, they appear as very smooth functions of the bubble radius. This rules out that the 'dips' in figure 4.16 are caused by an anomaly in the viscous damping term in the model. This was very unlikely, since the position of the dip depends on pulse length and acoustic power. In figure 4.19(c) and 4.19(d) the resonance frequency, calculated by iteration of equations 2.42, 2.43 and 4.4, corresponding to the bubble radius where the effect reaches its minimum, is plotted against pulse duration and acoustic pressure. The resonance frequency decreases with both increasing pulse length and acoustic power. This result is as expected, since the resonance frequency is approximately proportional to $1/R$.

The dependence on pulse duration of $R_{\mathtt{min}}$ is very counterintuitive. Shorter pulses have a broader frequency spectrum, which means that at short pulses the main frequency peak will have more overlap with the resonance frequency peak. Also the overlap will increase with

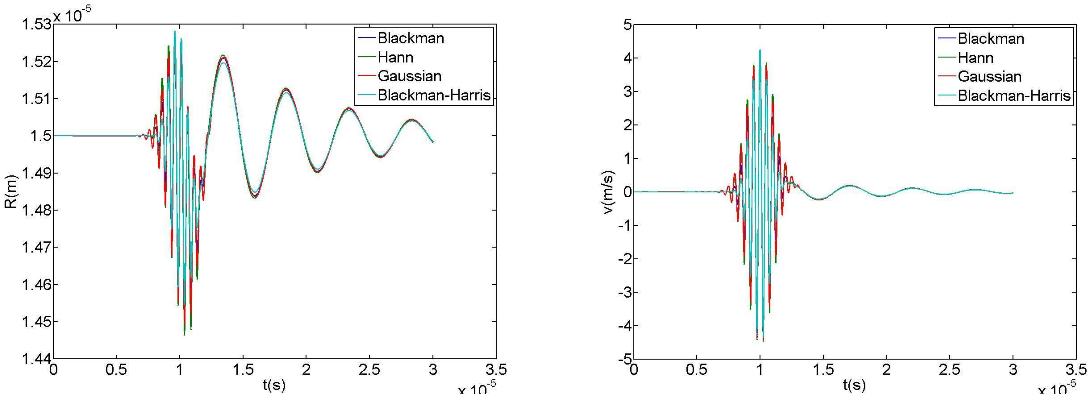

(a) bubble radius.

(b) wall velocity.

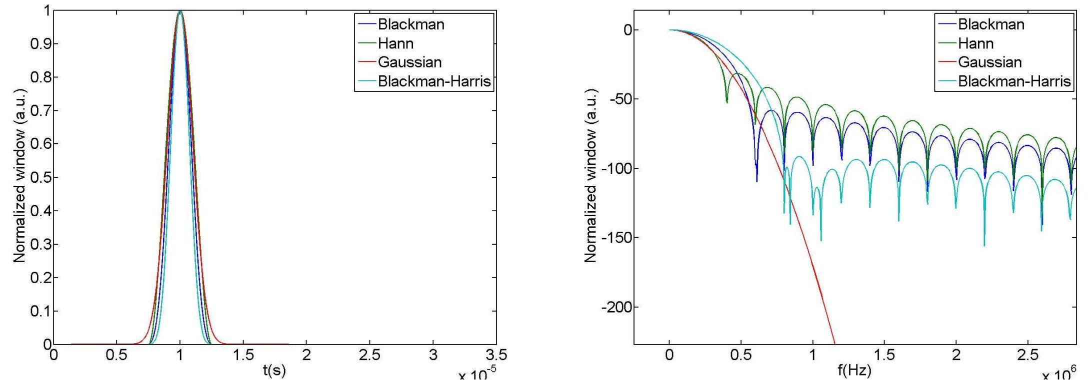

(c) window amplitude.

(d) window power spectrum.

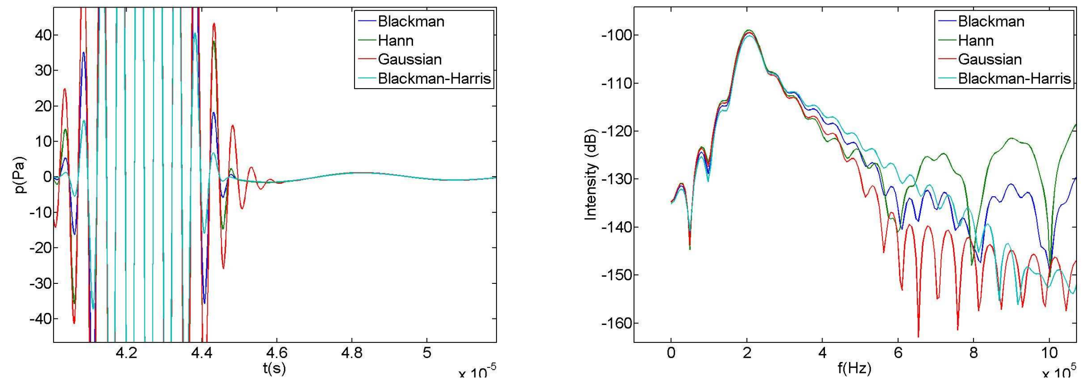

(e) scattered pressure.

(f) power spectrum.

Figure 4.15: Bubble radius, wall velocity, window characteristics, and scattered pressure as a function of time. The scattered pressure was normalized by the amplitude of the incident pulse. The incident pressure pulse had a duration of 5 μs, an amplitude of 0.8 MPa and a frequency of 2 MHz. The bubble radius was 15 μm.

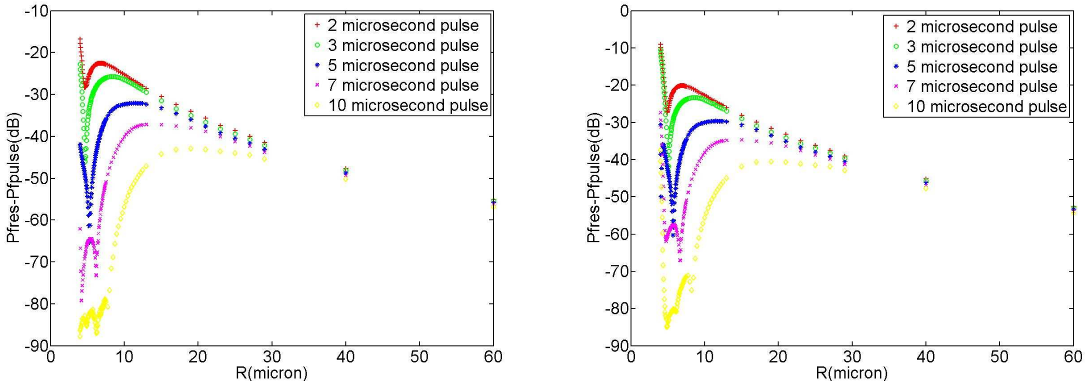

(a) $P_{ac} = 0.6$ MPa.

(b) $P_{ac} = 0.8$ MPa.

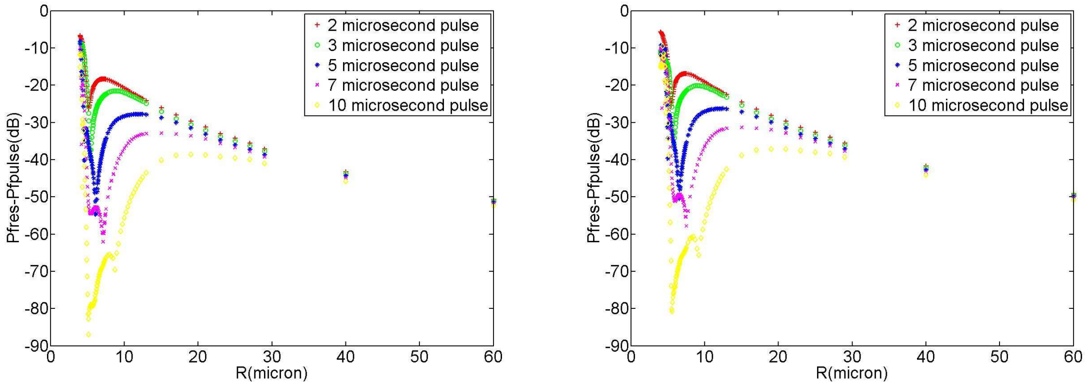

(c) $P_{ac} = 1.0$ MPa.

(d) $P_{ac} = 1.2$ MPa.

Figure 4.16: Ratio of the power at the bubble resonance frequency and the insonation frequency against bubble radius, for different burst lengths and acoustic pressures.

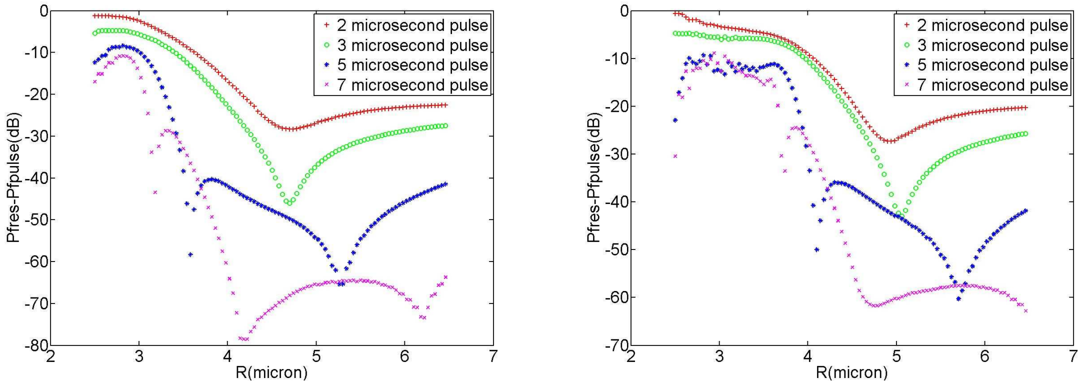

(a) $P_{ac} = 0.6$ MPa.

(b) $P_{ac} = 0.8$ MPa.

Figure 4.17: Ratio of the power at the bubble resonance frequency and the insonation frequency against bubble radius, for different burst lengths and acoustic pressures, zoomed in on small radii.

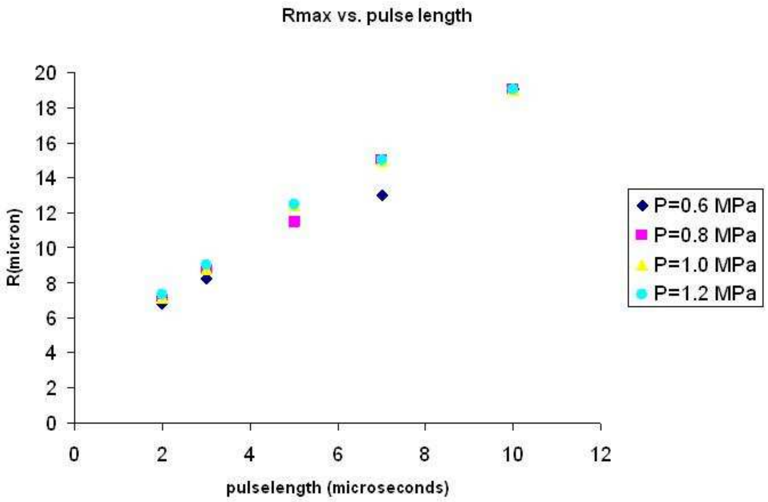

(a) $R_{\max}$ versus pulse length.

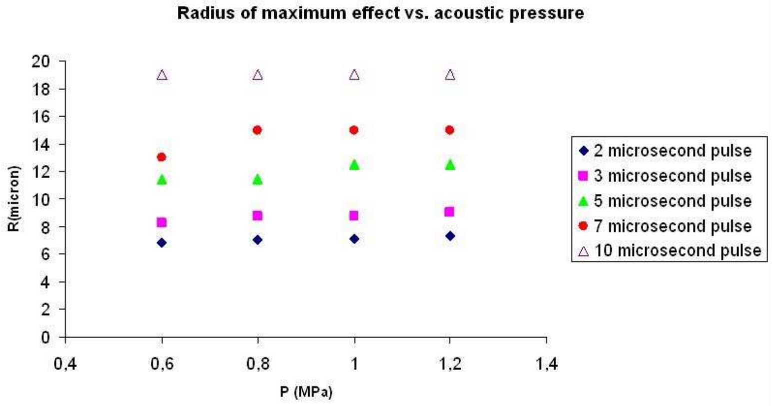

(b) $R_{\max}$ versus acoustic pressure.

Figure 4.18: Radius at which the relative power at the resonance frequency has a maximum ($R_{\mathtt{max}}$) plotted against pulse duration and acoustic pressure.

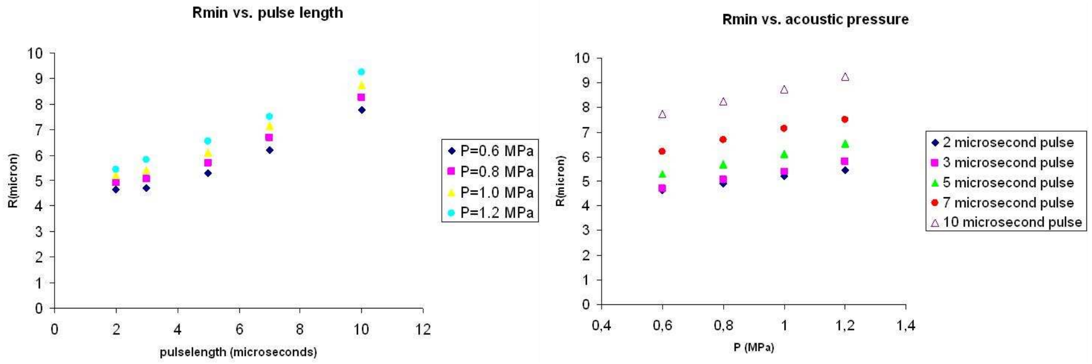

(a) $R_{\mathtt{min}}$ versus pulse length.

(b) $R_{\mathtt{min}}$ versus acoustic pressure.

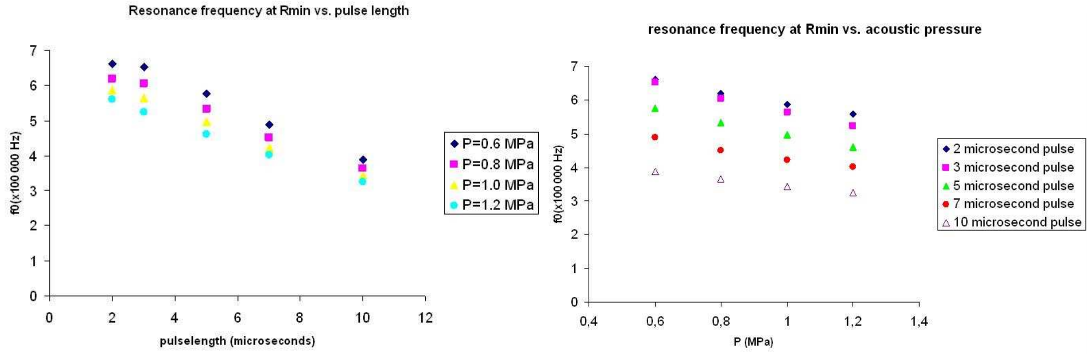

(c) resonance frequency at $R_{\mathtt{min}}$ versus pulse length.

(d) resonance frequency at $R_{\mathtt{min}}$ versus acoustic pressure.

Figure 4.19: Radius and corresponding resonance frequency at which the relative power at the resonance frequency has a minimum ($R_{\mathtt{min}}$) plotted against pulse duration and acoustic pressure.

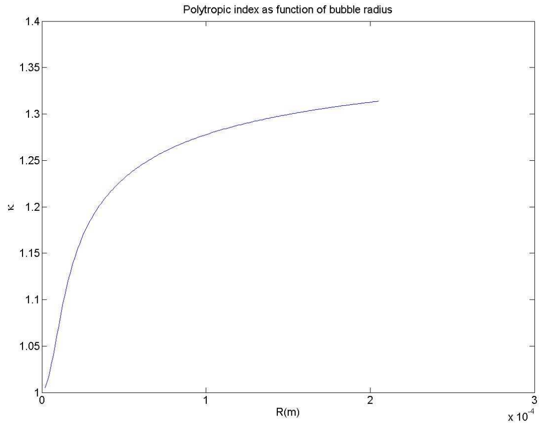

(a) polytropic constant versus bubble radius

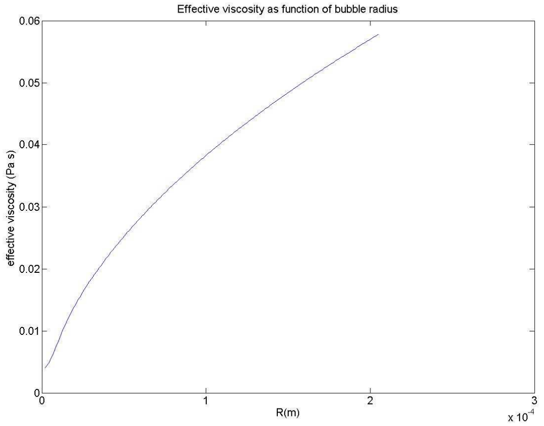

(b) effective viscosity versus bubble radius

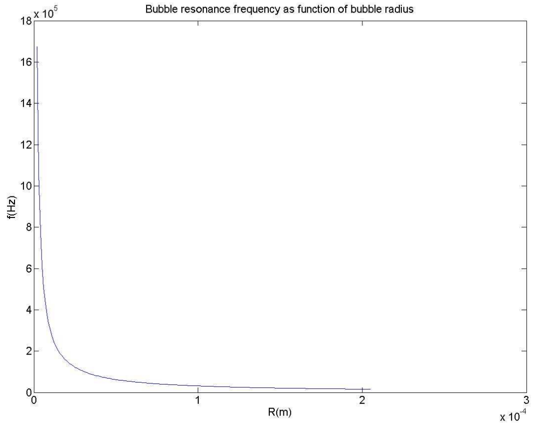

(c) resonance frequency versus bubble radius

Figure 4.20: Polytropic constant, effective viscosity and resonance frequency as function of bubble radius, calculated by iteration of equations 4.4, 2.42 and 2.43.

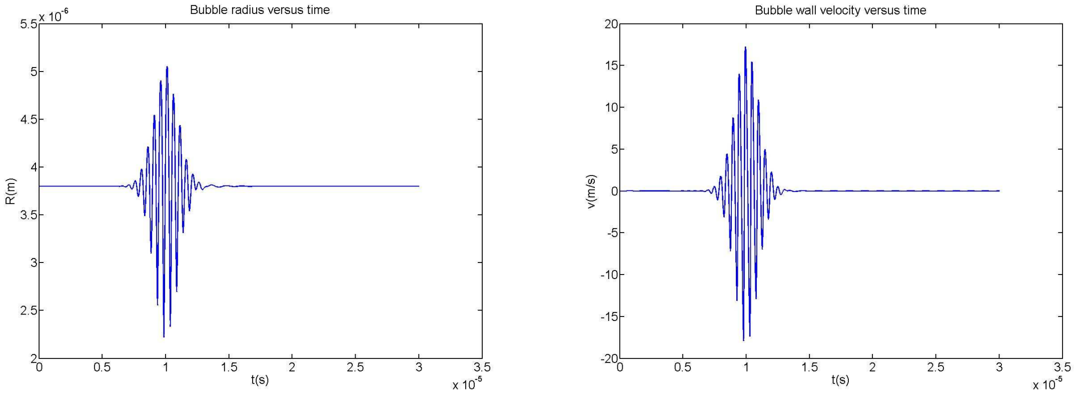

(a) bubble radius. (b) wall velocity.

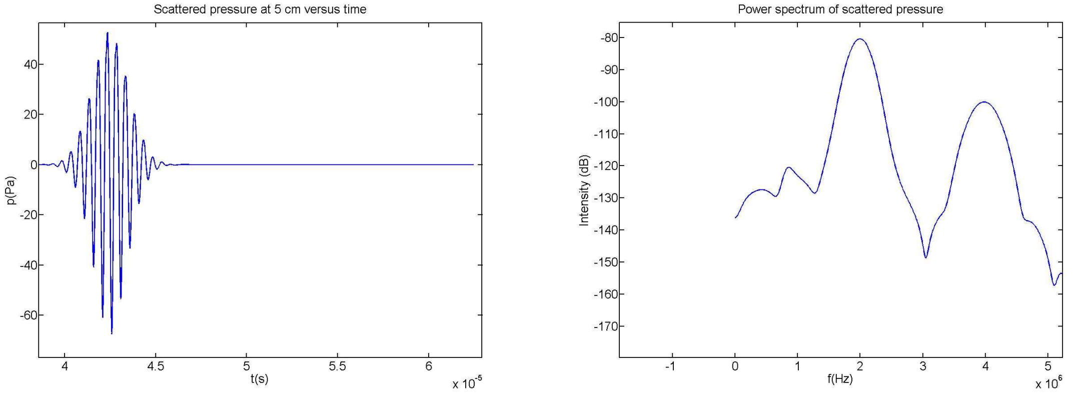

(c) scattered pressure. (d) power spectrum.

Figure 4.21: Bubble radius, wall velocity, and scattered pressure as function of time for a bubble with a radius of 3.8 $\mu\mathtt{m}$. The incident pressure pulse had a duration of 5 $\mu\mathtt{s}$, an amplitude of 0.6 MPa, and frequency of 2 MHz.

decreasing radius. If there is a critical value for the overlap, the critical radius ($R_{\mathtt{min}}$) will increase with decreasing pulse length. However, from figure 4.19 it is obvious that simulations show an opposite tendency. This can possibly be explained by the fact that shorter pulses also carry less energy.

Another possibility to explain the anti-resonances is a phase effect. The effect of the start and end of the pulse could cancel each other when a certain pulse length is used. However, this will not be very probable because in that case there would be no 'dip' for some pulse lengths, since the pulse length should be a exactly $(2k+1)/2$ times the period of one oscillation at the resonance frequency. To investigate this more thoroughly the bubble radius, wall velocity and scattered power are shown for different bubble sizes, e.g. at $R_{\mathtt{max}}$, at $R_{\mathtt{min}}$ and for very small bubbles, see figures 4.21, 4.22 and 4.23. The difference between especially the behaviour at $R_{\mathtt{max}}$ and $R_{\mathtt{min}}$ is striking. Whereas a bubble of size $R_{\mathtt{max}}$ shows oscillation at its resonance frequency, a bubble of size $R_{\mathtt{min}}$ hardly does. The exact explanation of this phenomenon remains unknown. It could be a kind of anti-resonance due to non-linearities in the Rayleigh-Plesset equation, assumptions in the model used, or a subtle interplay between the pulse

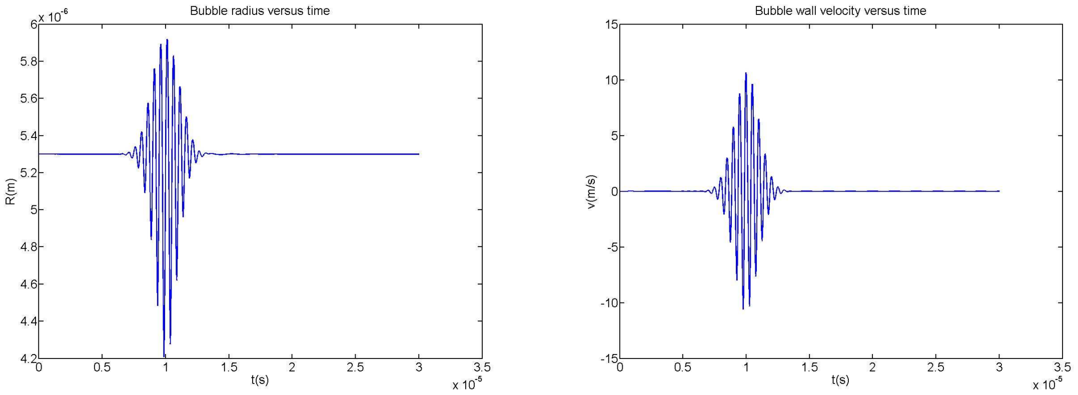

(a) bubble radius.

(b) wall velocity.

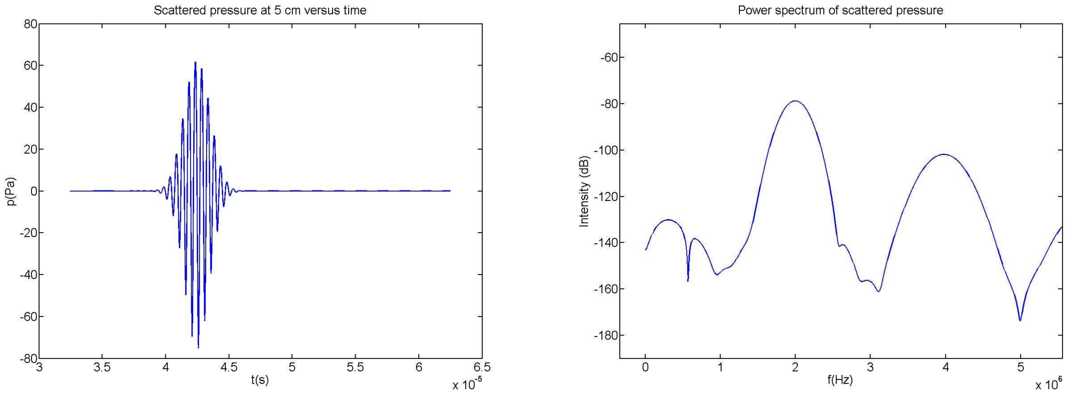

(c) scattered pressure.

(d) power spectrum.

Figure 4.22: Bubble radius, wall velocity, and scattered pressure as function of time for a bubble with a radius of 5.3 μm. The incident pressure pulse had a duration of 5 μs, an amplitude of 0.6 MPa, and frequency of 2 MHz.

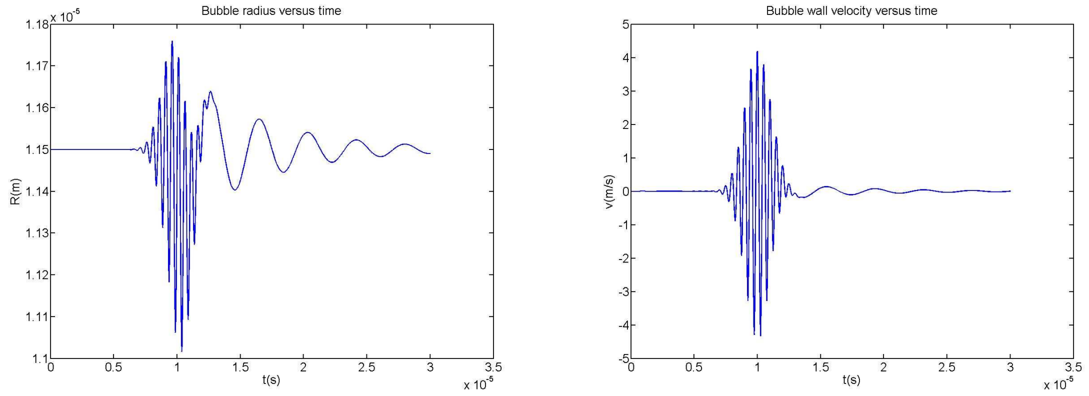

(a) bubble radius.

(b) wall velocity.

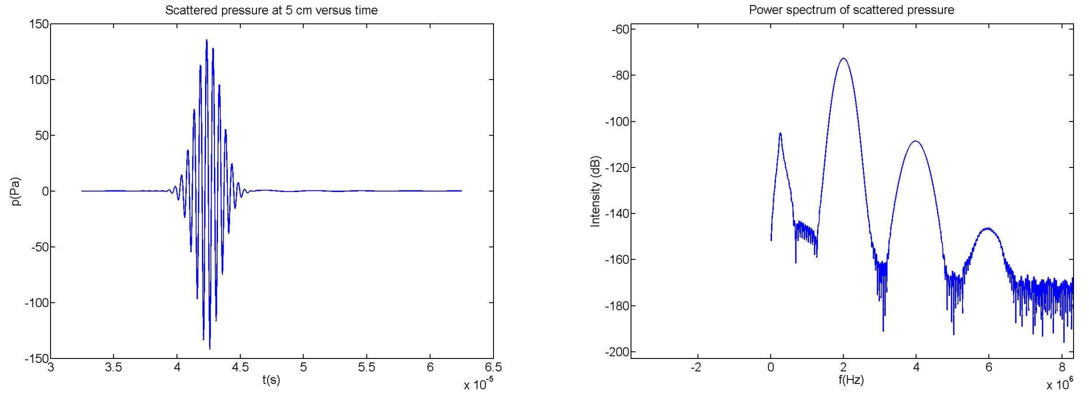

(c) scattered pressure.

(d) power spectrum.

Figure 4.23: Bubble radius, wall velocity, and scattered pressure as function of time for a bubble with a radius of 11.5 μm. The incident pressure pulse had a duration of 5 μs, an amplitude of 0.6 MPa, and frequency of 2 MHz.

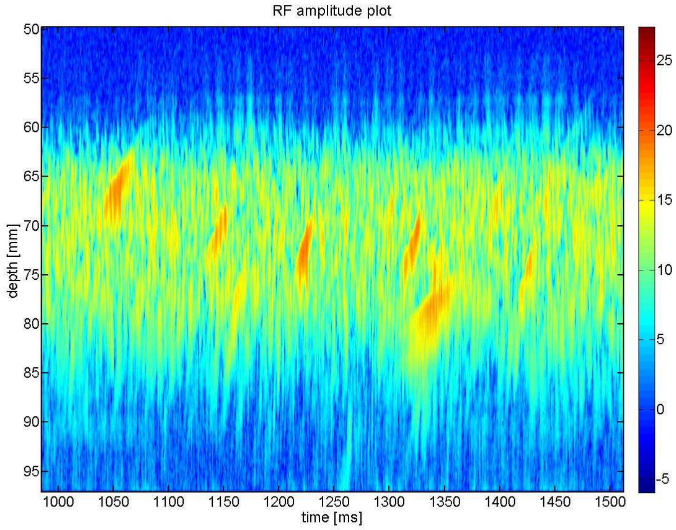

Figure 4.24: Several MES visible in an RF amplitude plot recorded after introducing 50 μm particles in the flow phantom. 5 MES are clearly visible, 2 are doubtful.

and resonance frequency of the bubble. It is unlikely that it follows from a numerical error, since the 'dips' are so well defined and are dependent of pulse duration and amplitude. An experimental study could shed new light on this problem.

4.4 Flow Phantom Experiments

To explore the limits of detection for small emboli using ultrasound, first small particles (with a diameter of 50 ± 20 μm) were introduced in the flow phantom setup described in the previous chapter. After the particles were allowed to travel through the setup several recordings were made. During the recordings also the Doppler audio signal was audible. It proved fairly difficult for human observers as well as the commercial detection algorithm of the Doppler device to detect the particles. However, some high intensity transient signals (HITS) were audible. The observation of those HITS was also the trigger to start recording RF data.

In the RF amplitude plots the MES are present as the typical shapes shown in previous sections. However, their amplitude has a level close to that of the blood speckle (variations in intensity due to density variations of erythrocytes in blood), as seen in figure 4.24. This complicates the automated detection of those MES, as the shape of the MES is not as smooth as the shape of more intense MES. The calculated embolus to blood ratio of 52 MES found in the amplitude plots varied between 2.5 and 8 dB with an average of 5.5 and a standard deviation of 1.5 dB. The duration of the MES varied between 10 and 90 milliseconds. There was no apparent correlation between MES duration and EBR (figure 4.25).

After the arterial filter was allowed some time to filter most particles out of the flow, larger particles were introduced, with a diameter of, in order: < 300, $300 - 425$ and > 425 μm. As expected this resulted in more intense MES, as seen in figure 4.26. For particles larger than $300\,\mu m$ the backscattered pressure exceeded the dynamic range of the ADC, which means that EBR calculations for those particles are no longer valid.

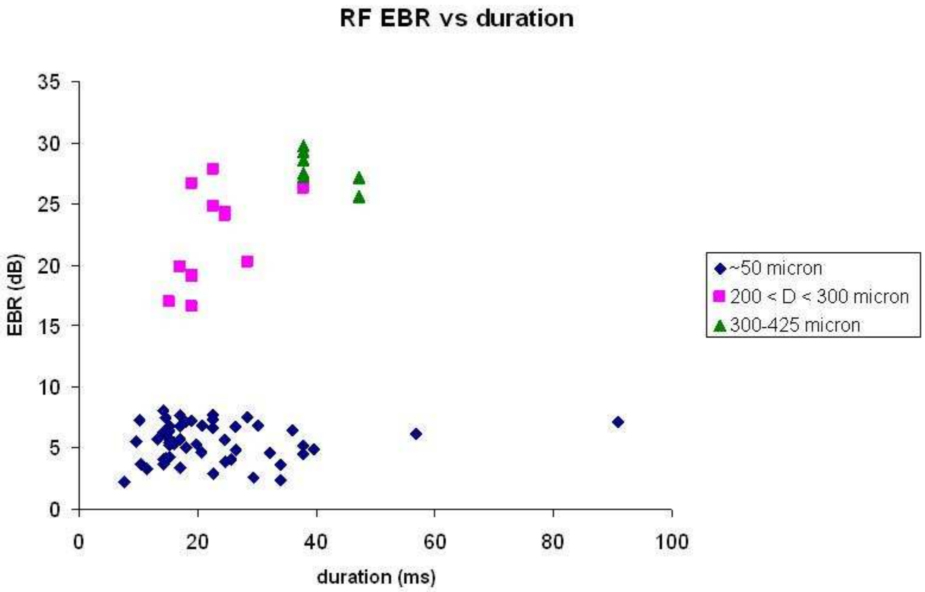

Figure 4.25: Scatter plot of calculated MES EBR and MES duration, recorded using the flow phantom set-up.

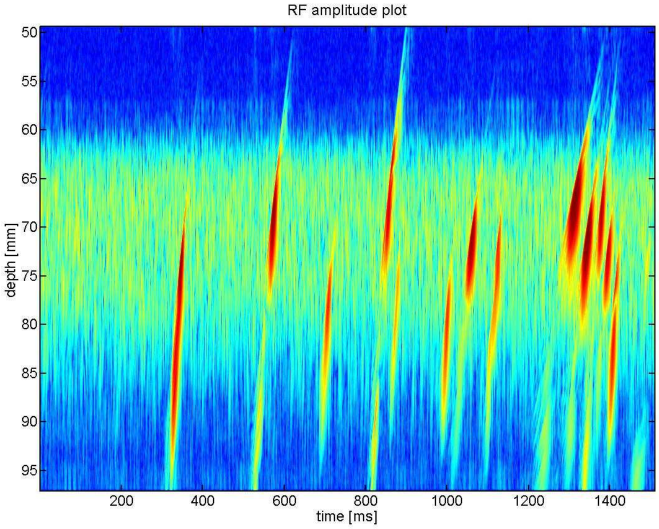

Figure 4.26: Several MES visible in an RF amplitude plot recorded after introducing $200 - 300$ μm particles in the flow phantom.

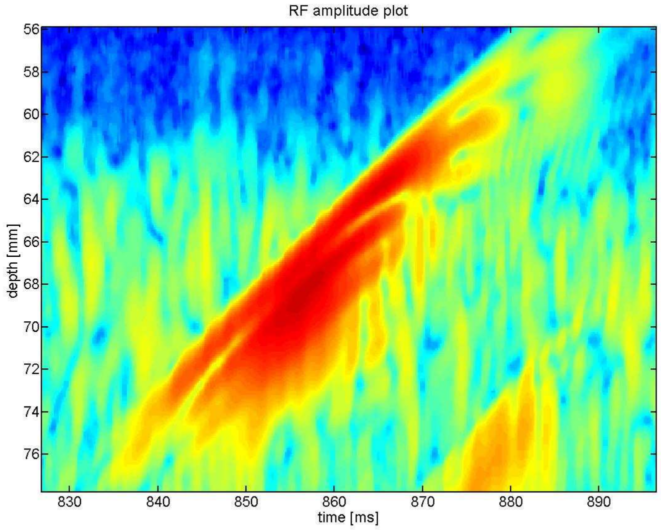

Figure 4.27: Single MES with clear reflections.

An important disadvantage of using tubing for the flow phantom is the possibility of reverberations in the wall. This can bee seen in figure 4.27. The distance in depth between the reflections is approximately 2.5 mm, which corresponds to a wall thickness of 1.25 mm. The thickness of the tubing used is indeed around 1.25 mm.

Chapter 5

Conclusion and Recommendations

It was already known that the clutter filtered RF amplitude plot is an alternative and possibly more useful method for emboli detection. However, several hurdles have to be taken to make this method suitable for clinical use. First of all the data stream is larger because of the high frequency signals. The data stream depends on the PRF, the depth window, and the dynamic range of the ADC. For a 12 bits ADC, a depth window of 800 points ($\approx$ 30 mm), and a pulse repetition frequency of 5 kHz, 7 MB of data will be acquired per second. With the current developments in hardware this should no longer be a problem. The operations that have to be performed on the signal to make it suitable for emboli detection are not so complicated that vast computational power is required. Moreover, an intelligent shape recognition and detection algorithm has to be developed. The physical properties of MES in RF plots are such that artifact rejection and detection with reasonable sensitivity should be possible.

This means that the road is clear for the advantages and possibilities of the RF method. First of all it can provide a method of quantifying vast emboli showers, whereas current commercial devices all fail at this point. The algorithm developed in this project showed that a sensitivity of 0.7 can already be achieved. Although this does not seem very impressive, it is an improvement compared to existing devices by at least an order of magnitude. Furthermore, a substantial part of the MES in the recordings had a very low intensity, below the detection threshold of the counting algorithm. Together with the fact that the algorithm can be improved in several ways, this shows that in quantifying emboli showers RF based detection can substitute existing Doppler based detection. Some of the advantages are a high temporal resolution in the order of 10 to 20 ms, depending on the pulse repetition frequency, the possibility of counting in the absence of human observers, and real time estimation of the embolic load. The resolution is improved because of the 2 dimensional nature of the method, and because of the fact that existing algorithms have a 'dead' time of approximately 50 to 100 ms after an event is detected. The absence of human observers has a very important economical advantage, since operations can last several hours, not to mention the fact that listening and counting emboli is a very boring task. Although emboli detection is in principle passive and detection will be several seconds after their origin, real-time detection will be important, to let the surgeon know that something is causing emboli.

A second advantage is the possible distinction between gaseous and solid emboli. As shown in figure 4.14, according to a theoretical model, bubbles of a certain range of radii will oscillate at their resonance frequency after the driving pulse ended. This means that the normal, FDA approved, 2 MHz pulse frequency can be used, with its advantages (lower noise level,

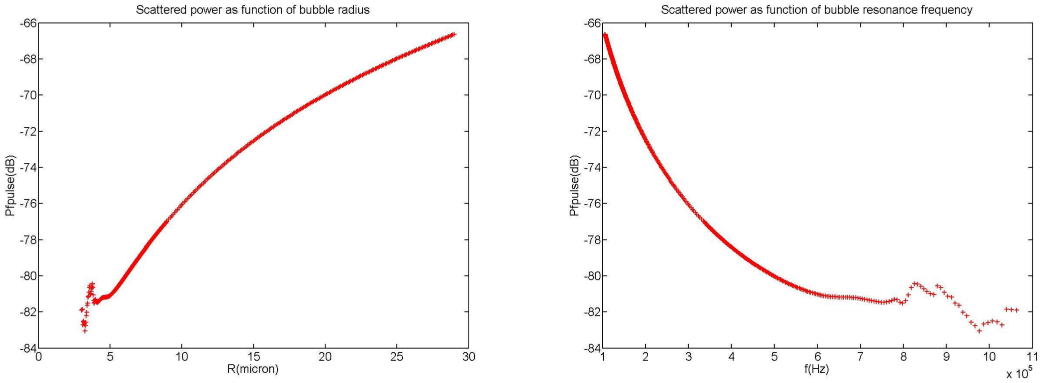

(a) Scattered power versus bubble radius

(b) Scattered power versus bubble resonance frequency

Figure 5.1: Scattered power relative to insonation power versus bubble radius and resonance frequency. The pulse length used in the simulations was 4 microseconds and the insonation power was 0.8 MPa.

possibility to detect also solid emboli). The resonance frequency can now be detected using a second transducer, which is used as recorder only. This transducer should have a sensitive frequency range of 100 to 400 kHz, so that bubbles of 8 to 30 μm radius can be detected. The intensity of larger bubbles is assumed to be so high that they can be classified as gaseous based solely on intensity. According to equation 2.19 solid scatterers should have a radius of approximately 150 μm to have an intensity close to gas bubbles of 30 micron ($-65\,$dB, see figure 5.1), which is very large for solids. Before any plans can be made for the development of a device like this, first the theoretical model has to be verified experimentally, to see whether the amplitude of the oscillations at the resonance frequency is high enough to be detected. Furthermore, so far many assumptions have been made. The influence of the skull, for instance, has been neglected. In conclusion, a lot of research has to be done before this method can be implemented in any device.

A third possible application is the detection of very low intensity MES. As seen in figure 4.24, using RF amplitude plots low intensity MES with an amplitude in the order of blood speckle amplitude can be detected. The problem here, however, lies in the fact how they can be distinguished from the speckle. In figure 4.24 it can be seen too that the speckle causes the MES shape to become less smooth, which means that the algorithm used to count during showers will have to be modified if it is to be used to detect low intensity MES. A possible solution is to use a very rigorous smoothing filter. The only characteristic that separates those low intensity MES from speckle is their duration. Speckle only lasts milliseconds, while MES have a duration (depending on velocity and insonation angle) of $10\,ms$ or more. Nevertheless, it will be difficult to distinguish very low intensity MES from blood speckle.

In general it can be said that RF based emboli detection offers many possibilities, and deserves further research, possibly followed by implementation in a commercial device.

Bibliography

[1] http://www.clinic-clinic.com/prclnc-mdcne/antmy/CNS/seciii10.jpg.

[2] Burckhardt Ch.B. Speckle in ultrasound b-mode scans. *IEEE Transactions on Sonics and Ultrasonics*, 25(1):1–6, 1978.

[3] Evans D.H. and Gittins J. Limits of uncertainty in measured values of embolus-to-blood ratios in dual-frequency tcd recordings due to nonidentical sample volume shapes. *Ultrasound in Medicine and Biology*, 31(2):233–242, 2005.

[4] Evans D.H. and McDicken W.N. *Doppler Ultrasound: Physics, Instrumentation and Signal Processing*, chapter 3. Wiley Sons, 2000.

[5] Brands P. et al. A radio frequency domain complex cross correlation model to estimate blood flow velocity and tissue motion by means of ultrasound. *Ultrasound in Medicine and Biology*, 23(6):911–920, 1997.

[6] Cowe J. et al. Rf signals provide additional information on embolic events recorded during tcd monitoring. *Ultrasound in Medicine and Biology*, 31(5):613–623, 2005.

[7] Cowe J. et al. Automatic detection of emboli in the tcd rf signal using principal component analysis. *Ultrasound in Medicine and Biology*, 32(12):1853–1867, 2006.

[8] Li S. et al. Nonlinear propagation in doppler ultrasound. *Ultrasound in Medicine and Biology*, 19(5):359–364, 1993.

[9] Markus H.S. et al. Intercenter agreement in reading doppler embolic signals. *Stroke*, 28:1307–1310, 1997.

[10] Moehring M. et al. Sizing emboli in blood using pulse doppler ultrasound i: Verification of the ebr model. *IEEE Transactions on Biomedical Engineering*, 43(6):572–580, 1996.

[11] Muth C. et al. Gas embolism. *The New England Journal of Medicine*, 342(7):476–482, 2000.

[12] Neville M.J. et al. Similar neurobehavioral outcome after valve or coronary artery operations despite differing carotid embolic loads. *Cardiovascular Surgery*, 121(1):125–136, 2001.

[13] Palanchon P. et al. Subharmonic and ultraharmonic emissions for emboli detection and characterization. *Ultrasound in Medicine and Biology*, 29(3):417–425, 2003.

[14] Pugsley W. et al. The impact of microemboli during cardiopulmonary bypass on neurophychological functioning. *Stroke*, 25:1393–1399, 1994.

[15] Russell D. et al. Online automatic discrimination between solid and gaseous cerebral microemboli with the first multifrequency transcranial doppler. *Stroke*, 33(8):1975–1980, 2002.

[16] Smith J. et al. A comparison of four methods for distinguishing doppler signals from gaseous and particulate emboli. *Stroke*, 29:1133–1138, 1998.

[17] T.G. Leighton. *The Acoustic Bubble.* Academic Press, 1994.

[18] Moehring M. and Klepper J.R. Pulse doppler ultrasound detection, charaterization and size estimation of emboli in flowing blood. *IEEE Transactions on Biomedical Engineering*, 41:35–43, 1994.

[19] Shutilov V.A. *Fundamental Physics of Ultrasound*, pages 198–209. CRC Pr Llc, 1988.

[20] Lanz T. von and Wachsmuth W. *Praktische Anatomie.* Number 1b. Springer, 1979.

[21] Mess W. Microembolic signal description: A reappraisal based on a customized digital post-processing system. *Ultrasound in Medicine and Biology*, 28(11):1447–1455, 2002.